Angiogenesis (2025) 28:17
https://doi.org/10.1007/s10456-025-09970-y

ORIGINAL PAPER

Cxcl9 modulates aging associated microvascular metabolic and angiogenic dysfunctions in subcutaneous adipose tissue

Xin Fu[1,2] · Yu Zhao[1,2] · Xiwei Cui[1,2] · Siyuan Huang[3] · Yanze Lv[4] · Chen Li[1,2] · Fuxing Gong[1,2] · Zhigang Yang[1,2] · Xiaonan Yang[4] · Ran Xiao[1,2]

Received: 29 October 2024 / Accepted: 2 February 2025 / Published online: 11 February 2025

Abstract
Microvascular aging, predominantly driven by endothelial cells (ECs) dysfunction, is a critical early event in cardiovascular diseases. However, the specific effects of aging on ECs across the microvascular network segments and the associated mechanisms are not fully understood. In this study, we detected a microvascular rarefaction and a decreased proportion of venular ECs in the subcutaneous adipose tissue of aged mice using light-sheet immunofluorescence microscopy and single-cell RNA sequencing. Moreover, aged ECs, especially in the venular subtype, exhibited a pseudotemporal transition to a terminal state characterized by diminished oxidative phosphorylation and strengthened cytokine signaling. Metabolic flux balance analysis predicted that among the 13 differentially expressed cytokines identified in aged EC subpopulations, Cxcl9 was strongly correlated with impaired oxidative phosphorylation in aged ECs. It was further validated using microvascular ECs treated with Cxcl9. Notably, the G protein-coupled receptor signaling pathway was subsequently suppressed, in which Aplnr suppression was also observed in aged ECs, contributing to their impaired energy metabolism and reduced angiogenesis. Based on these findings, we propose Cxcl9 as a biomarker for aging-related dysfunction of microvascular ECs, suggesting that targeting Cxcl9 signaling may help combat microvascular aging.

Keywords Microvascular aging · Endothelial cells · Metabolism · Cxcl9 · Aplnr · Angiogenesis

Introduction

Vascular aging involves pathological changes in the macrovascular and microvascular systems, mainly characterized by arterial and arteriolar stiffness, loss of vascular density, and endothelial dysfunction [1]. Previous research primarily emphasized the impact of aging-related cardiovascular risk factors on large vessels (e.g., arteriosclerosis, atherosclerosis, and vascular occlusive events), with less attention paid to the microvasculature [2]. However, microvascular dysfunction is considered the earliest marker of cardiovascular disease, which contributes to the pathogenesis of several age-related diseases [3, 4]; these facts highlight the importance of understanding and managing microvascular health in the context of aging. The microvascular endothelium, comprising a monolayer of endothelial cells (ECs), is a vital regulator of microvascular homeostasis [5]. In addition to their barrier functions, ECs produce factors crucial for vascular tone, angiogenesis, barrier permeability, and inflammatory responses [3]. EC dysfunction is a major aspect and key mechanism underlying age-related microvascular impairment [6].

The microvascular network, composed of small arteries, arterioles, capillaries, and venules with diameters < 150–200 μm, is the final conduit of the cardiovascular system, responsible for local blood perfusion and the exchange of

Xin Fu, Yu Zhao and Xiwei Cui contributed equally to this work.

✉ Ran Xiao
xiaoran@psh.pumc.edu.cn

1 Research Center of Plastic Surgery Hospital, Chinese Academy of Medical Sciences and Peking Union Medical College, Beijing 100144, P. R. China

2 Key Laboratory of Tissue and Organ Regeneration, Chinese Academy of Medical Sciences, Beijing, P. R. China

3 Academy for Advanced Interdisciplinary Studies, Peking University, Beijing 100871, P. R. China

4 Department of Hemangioma and Vascular Malformation of Plastic Surgery Hospital, Chinese Academy of Medical Sciences and Peking Union Medical College, Beijing 100144, P. R. China

gases and metabolites [7]. Moreover, this network plays a crucial regulatory role in immune and inflammatory responses and modulates organ function because of its direct contact with parenchymal cells [8]. The age-related decline in endothelial function is marked by reduced angiogenic capacity, decreased nitric oxide (NO) production, and enhanced expression of adhesion molecules that promote leukocyte recruitment [9]. Few previous reports reflect morphological changes in aged microvasculature across multiple organs, including thinning of brain capillary ECs [10], age-related pseudocapillarisation with the defenestration of the hepatic sinusoidal endothelium [11], and capillary loss with impaired EC proliferation and NO production in aged kidneys [12, 13]. Recently, aged mice were reported to exhibit capillary loss due to insufficient vascular endothelial growth factor (VEGF) signaling [14]. With the advances in single-cell sequencing, transcriptomic landscapes of vascular ECs aging in different tissues and species have been reported at single-cell level, such as aortas and coronary arteries in cynomolgus monkeys [15], cerebral microvascular ECs in mouse [16, 17], vasculature in mouse skin [18]. However, the precise molecular changes induced by age-related challenges in ECs across different organs and vascular beds remain poorly understood.

The pathophysiological mechanisms underlying age-dependent EC dysfunction are multifactorial, involving inflammation as the fundamental pathological process [19]. Inflammaging refers to the chronic, low-grade inflammation that develops with aging, and is characterized by enhanced circulating levels of pro-inflammatory cytokines [20]. The circulating inflammatory cytokines can activate the proinflammatory transcription factor NFκB in ECs, contributing to endothelial dysfunction such as senescence and oxidative stress [21, 22], which further exacerbates age-related vascular inflammation and impairment [1, 23]. In recent decades, the interplay between inflammation and metabolic changes in ECs has been increasingly recognized [24]. For instance, excess glycolysis in ECs has been reported to promote NF-kB-driven vascular inflammation via lactate signaling [25]. Deficiency in isocitrate dehydrogenase 2 (IDH2), which controls redox homeostasis in ECs, can induce inflammation via mitochondrial oxidative stress [26]. Disruptions in glucose [27], fatty acid [28], and folate [29] metabolisms can promote EC senescence, which is an important risk factor for age-related CVD [30]. Targeting the metabolic imbalances associated with inflammation may provide a strategy to control vascular aging. Nevertheless, the patterns and mechanisms underlying metabolic alterations in aged microvascular EC, and their correlation with the pro-inflammatory response of ECs remain unclear [30, 31].

Adipose tissue is a highly vascularized organ that serves as a biological driver of aging and age-related diseases [32]. The aging process of adipose tissue begins predominantly in subcutaneous adipose tissue (SAT) and is strongly associated with chronic inflammation [33]. A recent single-nucleus RNA-sequencing study from a combination of human visceral and SAT samples reported that $FKBP5^+$ ECs specifically reside in aged human adipose tissues, exhibit the potential for endothelial-to-mesenchymal transition, and play a critical role in regulating adipocytes [34]. However, the visceral and SAT exhibit different responses to aging [33], their combination may obscure the cellular dynamics and molecular signatures specific to aged SAT.

To explore the effects of aging on the SAT microvasculature, we collected inguinal subcutaneous fat from mice. Using single-cell RNA sequencing and light-sheet immunofluorescence microscopy, we discovered a structural deficiency in microvascular network architecture. This deficiency was associated with a decreased proportion of venular ECs within the overall EC population. Using various biostatistical analytical techniques, we illustrated the pseudotemporal transition of aged ECs towards a terminal state characterized by reduced energy metabolism and increased cytokine signaling, particularly within the venular subtype. This metabolic alteration was closely linked to the elevated production of the inflammatory chemokine Cxcl9 and the consequent downregulated expression of Aplnr in aged ECs. Our findings provide new insights into the phenotypic alterations and mechanisms underlying age-related microvascular remodeling, highlighting the impact of inflammation on endothelial dysfunction through the modulation of EC metabolism.

Materials and methods

Animals

Wild type female C57BL/6 N mice were purchased in Beijing Vital River Laboratory Animal Technology Co., Ltd and housed at the animal laboratory in plastic surgery hospital of Chinese Academy of Medical Sciences at SPF environment. Standard rearing condition: room temperature 20 ± 2℃, 50–60% humidity, 12 h light-dark lighting cycle, fed chow diet purchased from Keao Xieli Feed Co. Ltd (Cat. no. 1016706714625204224). Distilled water and diet were available ad libitum. All experiments were approved by the Institutional Animal Care and Use Committee of Plastic Surgery Hospital (Institute). Young group (3-month-old) and aged group (> 18-month-old) mice were used in this study. Body weight and body length of aged ($n = 10$) and young ($n = 5$) mice were measured and the Lee obesity index was calculated as LOI=$\sqrt[3]{}$(body weight (kg)×1000)/(body length(cm)). The mice were fasted overnight, and their

blood glucose were measured using an Accu-chek active glucose meter (Roche, Basel, Switzerland). For glucose tolerance test, 1 mg/g glucose was administered intraperitoneally to mice that had been fasted overnight, and blood glucose levels were measured at 5-, 15-, 30-, 45-, 60-, 90- and 120-minutes post-injection. The blood glucose curve was plotted against time and the area under the curve was calculated.

Histology staining

SATs were fixed in 10% formalin (Sigma) overnight at 4 °C. Tissues were then incubated in 70% ethanol before embedding in paraffin sections and serial SAT sections were cut at 10-μm thickness. Consecutive sections were stained with H&E to analyze adipose tissue and microvascular morphology. After deparaffinization in xylene and rehydration through graded ethanol, sections were stained with hematoxylin for nuclear visualization, differentiated in acid alcohol, and blued in ammonia water. Eosin was then applied to stain cytoplasmic and extracellular components, followed by dehydration through graded ethanol, clearing in xylene, and mounting with a synthetic resin medium. Slides were observed under a light microscope (Leica).

Multiplex immunofluorescence staining of tissue

Tissue sections were fixed in 4% paraformaldehyde (PFA) and subjected to antigen retrieval to unmask epitopes. Antigen retrieval was achieved by heating the sections in EDTA buffer (P0085, Beyotime, China) at 95–100 °C for 15 min using a microwave. After cooling to room temperature (30 min to 1 h), the sections were incubated with 3% hydrogen peroxide for 10 min to eliminate endogenous peroxidase activity. They were then sequentially rinsed in PBS and PBS-T solutions. Subsequently, the sections were incubated with 0.5% Triton X-100 for 10 min to enhance permeability. Blocking was performed using a blocking buffer (5% goat serum in PBS-T) for 1 h at room temperature (RT) to prevent nonspecific binding. The sections were then incubated overnight at 4 °C with rabbit anti-mouse Cxcl9 polyclonal antibody (PAB928mu01, Cloud-Clone Corp) and rat anti-mouse CD31 monoclonal antibody (550274, BD Pharmingen) simultaneously. Following overnight incubation, sections were stained with Goat Anti-rabbit IgG H&L Alexa Fluor® 488 (ab150077, Abcam) and Goat Anti-rat IgG H&L Alexa Fluor® 568 (ab175476, Abcam) for 1 h at RT. Autofluorescence was removed using Vector® True VIEW™ Autofluorescence Quenching Kit (SP-8400, Vectorlabs). Hoechst 33,258 was used to stain cell nuclei, followed by mounting with an anti-fading mounting solution from the Vector kit for observation. Sections were captured using the SELLARIS confocal microscope (Leica Corporation). For image processing and analysis, LAS-X (Leica, ver 4.7.0) software was used.

Tissue immunohistochemistry staining

Tissue samples were first collected and fixed in 4% PFA to preserve morphology and antigenicity, followed by embedding in paraffin and sectioning into 4–5 μm slices using a microtome. The sections were mounted on glass slides, deparaffinized in xylene, and rehydrated through a graded ethanol series before rinsing in distilled water. To retrieve antigens, the sections were heated in EDTA buffer (P0085, Beyotime, China) at 95–100 °C for 15 min using a microwave. Once cooled to room temperature (30 min to 1 h), 3% hydrogen peroxide was applied for 10 min to remove endogenous peroxidase activity. Afterward, the sections were rinsed sequentially in PBS and PBS-T. To improve permeability, they were treated with 0.5% Triton X-100 for 10 min. Finally, nonspecific binding was blocked by incubating the sections with blocking buffer (5% goat serum in PBS-T) for 1 h at RT. The tissue was then incubated with a specific primary antibody diluted in same buffer overnight at 4 °C. Different targets were labeled using specific antibodies, including Ki-67 rabbit anti-mouse primary antibody (GB111141, Servicebio), $p16^{INK4a}$ rabbit anti-mouse primary antibody (10883-1-AP, Proteintech), and Anti-Ackr1 rabbit anti-mouse primary antibody (PA5112940, Thermo Scientific). After rinsing with PBS and PBS-T, the slides were treated with Goat Anti-Rabbit IgG/HRP-conjugated secondary antibody (SE134, Solarbio) for 1 h at room temperature. For chromogenic detection, a DAB (3,3′-diaminobenzidine) kit (AR1027-3, Boster) was used to visualize the antigen-antibody complex. Chromogenic slides were counterstained with hematoxylin to visualize nuclei before mounting with coverslips. Finally, the slides were observed under an Olympus BX53 microscope (Olympus Corporation), with images captured for quantitative analysis.

TUNEL assay

The TUNEL assay was performed using the DAB (SA-HRP) TUNEL Cell Apoptosis Detection Kit (G1507, Servicebio, China). After deparaffinization and rehydration, the tissue sections were thoroughly washed with PBS. They were then permeabilized with proteinase K and treated with 0.5% Triton-X100 for membrane disruption. To inhibit endogenous peroxidase activity, the sections were incubated with 3% hydrogen peroxide. The sections were then incubated with a TUNEL reaction mixture containing terminal deoxynucleotidyl transferase (TdT) enzyme and labeled nucleotides, allowing the TdT enzyme to incorporate biotin-labeled

dUTPs into the 3'-OH ends of DNA fragments. After incubation, the sections were washed and treated with horseradish peroxidase (HRP)-conjugated streptavidin antibody. A substrate solution was then applied to visualize apoptotic cells as brown-stained nuclei under a light microscope. Counterstaining with hematoxylin was performed to highlight the tissue structure.

3D volume fluorescence imaging of SAT

The tissue processing and 3D volume fluorescence imaging of SAT were performed as previously reported in Tsinghua University [35]. Briefly, Mice were CO_2-euthanized and dissected. Hearts were exposed and 50 mL PBS was perfused through the left ventricle to clear blood, followed by 50 mL 4% PFA perfusion. Bilateral inguinal adipose tissues were harvested, washed with PBS, and fixed in 4% PFA for 24 h. Tissues were cleaned under a microscope and washed again before staining. Permeabilization was done with PBS containing 0.2% TritonX-100, 10% DMSO, 0.2% Deoxycholate, and 20 mM EDTA (pH 8.0) at 37 °C for 24 h, followed by a second step with PBS, 0.2% TritonX-100, 10% DMSO, and 100 mM glycine. Nonspecific binding was blocked with PBS supplemented with 0.2% TritonX-100, 10% DMSO, and 5% donkey serum at 37 °C for 24 h. Tissues were incubated with primary antibodies in PBS/0.2% Tween-20, 10 µg/ml heparin, 5% DMSO, and 5% donkey serum at 37 °C for 48 h, then washed five times for 2 h each with PBS/0.2% Tween-20 and 10 µg/ml heparin at room temperature. Alexa dye-conjugated secondary antibodies were applied similarly for 48 h, with overnight washes at 37 °C.

For staining process, CD31 (Cat#A04950, SAB) and Goat Anti-Mouse IgG H&L Alexa Fluor® 488 (ab150113, Abcam) were used to label the vessels in fluorescence imaging (Fig. 1c). After immunofluorescence staining, tissue clearing was performed based on optimized iDISCO method. Briefly, immunolabeled adipose samples were embedded in 1% agarose/PBS blocks. Blocks were dehydrated at RT with methanol (20-100%, 2 h each, except 100% twice for 1 h). Then, treated with dichloromethane/methanol (2:1) for 2 h, followed by 100% dichloromethane for 30 min twice. Blocks were cleared in 100% dibenzyl ether for 12 h (repeated) for 3D fluorescence imaging. The images were captured by Luxendo LCS SPIM light-sheet microscope and Zeiss Lightsheet 7 Light Sheet Fluorescence Microscopy. Imaris package (version 9.7 and version 10.0, Oxford Instruments Group) was used to trace and calculate the vasculature density. Briefly, three to six cubic volumes were selected from SAT, and immunolabeled vasculatures were manually traced. Student's two-sided t-tests were performed using GraphPad Prism (version 9.5, GraphPad Software).

Fig. 1 Aging alters the microvascular network in subcutaneous adipose tissue by primarily affecting EC functions. (**a**) Uniform manifold approximation and projection (UMAP) clustering of 15 cell types in mouse stromal vascular fraction (SVF) isolated from inguinal subcutaneous adipose tissue (SAT). Mac: Macrophage; DC, dendritic cell; pIC, proliferative immune cell; MC, mast cell; T, T cell; NK, Natural killer cell; B, B cell; PC, Plasma cell; APC, adipose progenitor and stem cell; EC, endothelial cell; SMC, smooth muscle cell; Epi, Epithelial cell; Schwann, Schwann cell; MyoEpi, Myoepithelial cell. (**b**) Heatmap showing gene expression signatures corresponding to each cell type. Left, columns represent individual cell types and rows indicate the expression of individual genes; the size of the dot represents cell number and the value for each gene presents the row-scaled Z score. Enriched GO terms for each cell type are presented (right). (**c**) Distribution of upregulated (red) and downregulated (blue) differentially expressed genes (DEGs) in different cell types in mouse SVF compared between the aged and young groups. Genes not differentially expressed are indicated in gray. The numbers of DEGs are indicated. The upper part (dotted lines) indicates the DEGs shared by at least two cell types, the lower panel indicates the unique DEGs of each cell type. The numbers of genes are annotated on the plots. (**d**) Longevity scores of every single cell in each cell type between aged and young SVF. ns, no significance, * $P<0.05$, ** $P<0.01$, and **** $P<0.0001$ by two-sided Wilcoxon rank-sum tests. (**e**) Representative images of the microvascular network in mouse SAT using immunofluorescence staining with CD31 antibody followed by light-sheet microscopy. The vasculature densities of SAT in both groups are calculated and compared. Data are presented as mean ± SEM; * $P<0.05$ based on Student's t test. Results were obtained from SAT of three mice from each group and three cubic volumes were selected from each SAT. Scale bar, 1000 µm. (**f**) Tube formation assay conducted using ECs isolated from mouse SAT. The total branching length and the number of meshes are measured and compared using Angiogenesis Analyzer plugin in ImageJ. Data are presented as mean ± SEM, * $P<0.05$ and ** $P<0.01$ based on Student's t test, two technical replicates were performed from 3 biological replicates for each group. (**g**) Characterization of cellular senescence of ECs isolated from young and aged mice SAT by SA-β-gal staining. The number of SA-β-gal positive cells is measured separately by assessing 2 randomly selected microscopic fields in each well using high-power magnification ($n=3$ per group) and data are presented as mean ± SEM; * $P<0.05$ based on Student's t test. Scale bar, 100 µm

Cell lines and primary cell culture

The mouse bEnd.3 cell line was purchased from ATCC. Primar microvascular ECs were isolated from mice inguinal SAT according to previously reported protocols [36]. Briefly, the harvested SAT was washed three times in PBS then minced with fine scissors until a homogeneous tissue suspension was obtained. The tissue suspension was incubated with collagenase NB4G (0.5 U/mL PBS) for 30 min to digest the tissue fragments. Excess fat chunks and single cells were removed using 500 µm and 20 µm filters successively, resulting in adipose tissue-derived microvascular fragments (ad-MVF). The obtained ad-MVF were seeded in Petri dishes with 15 mL Endothelial Cell Complete Medium (#PriMed-iCell-002, iCell Bioscience, China) to allow the

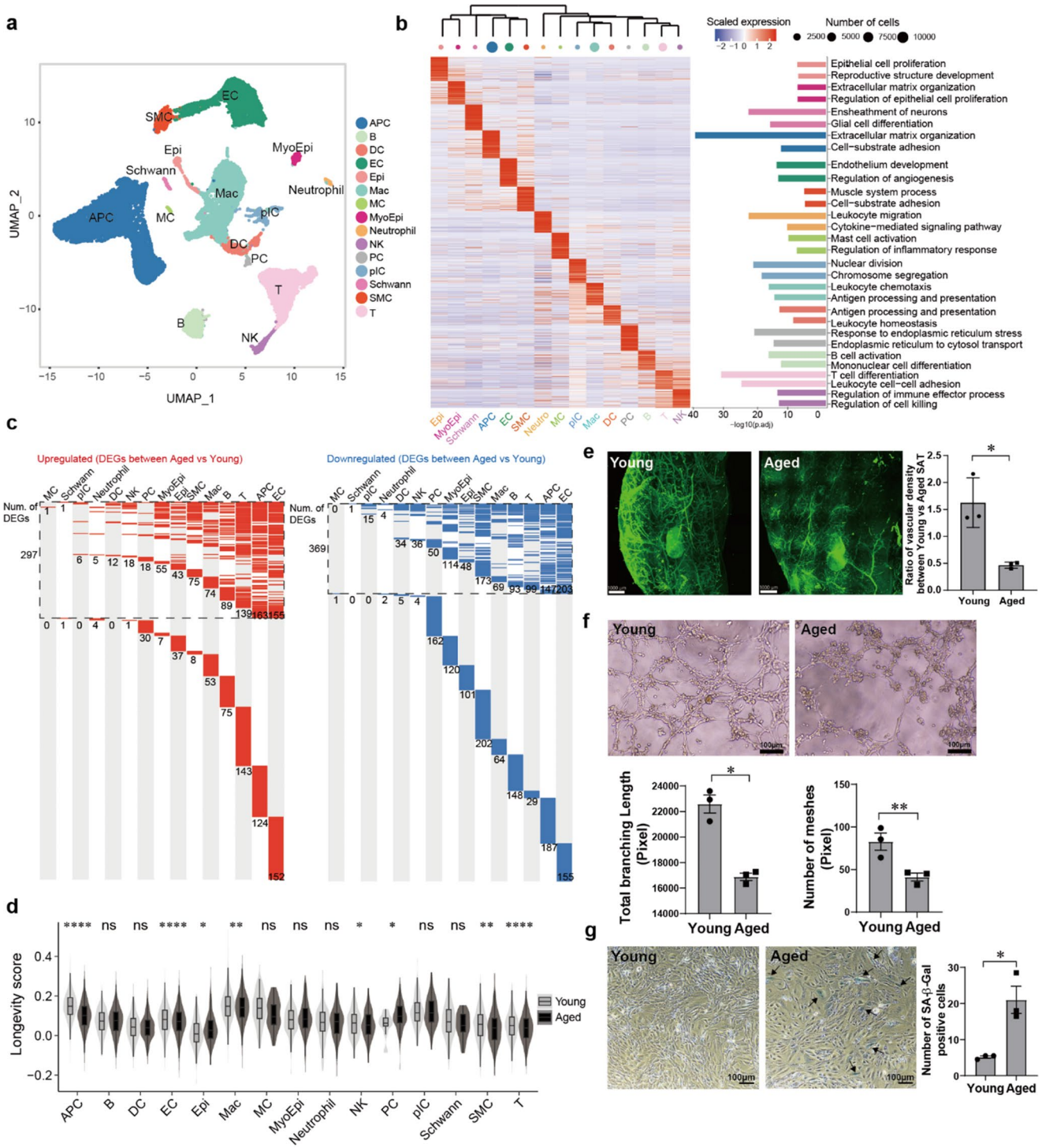

selective outgrowth and propagation of primary ECs from the vessel fragments. When cells reached around 90% confluency, they were detached from the culture plate by treating with 0.25% trypsin (0.02%EDTA) for 1 to 2 min and then transferred to new culture plate with 1:3 splitting ratio. Cells were maintained in endothelial cell medium (Sciencell 1001, ECM) under 5% CO2 at 37 °C in a humidified incubator.

Tube formation assay

Primary ECs at passage 2 were used for tube formation assay. Matrigel Basement Membrane Matrix (BD Biosciences) was diluted with ECM medium and coated in 24-well plates at 37 °C for 1 h. Then, 5×10^4 ECs were seeded in the ECM on Matrigel. The tube formation ability of ECs was

measured at 6 h. The number of meshes and total branching length of the tubular structures was quantified by ImageJ using plugin Angiogenesis Analyzer.

Senescence-associated β-galactosidase (SA-β-gal) staining

Primary ECs at passage 2 were washed once with PBS and fixed in SA-β-gal staining fix solution for 15 min at room temperature. Cells were then washed three times with PBS and incubated with SA-β-gal staining solution (C0602, Beyotime Biotechnology) for 16–20 h at 37 °C. After the overnight incubation, cells were washed with PBS and observed under a bright field microscope.

Tissue dissociation and adipose stromal vascular fraction (SVF) cells isolation

For single cell sequencing, inguinal subcutaneous adipose was carefully dissociated from young group ($n=4$) and aged group ($n=3$) female C57BL/6 N mice. Excised inguinal subcutaneous adipose was rinsed twice thoroughly with Dulbecco's Phosphate-Buffered Saline (DPBS, supplemented with 1% Penicillin-Streptomycin Solution), and then the hair stuck to the adipose tissue was removed carefully. The minced adipose tissues were digested with collagenase D (2 mg/ml, Roche) and collagenase type I (2 mg/ml, Gibco) in DMEM (Hyclone, USA) for 45 min at 37 °C incubator shaker. DNase-I (Sigma, USA) was added at 15 min and 30 min during digestion. The digestive mixture was quenched with DMEM supplemented with 10% FBS and filtered via 100 μm nylon filter, then centrifuged at 400×g for 5 min. Supernatant were discarded and the cell pellet was resuspended with red blood cell lysis buffer (Solarbio, China) for 3 min on the ice. The cell lysate was quenched with DMEM supplemented with 10% FBS and centrifuged at 400×g for 5 min. DPBS supplemented with 0.4% bovine serum albumin (Gibco, USA) was used to resuspend the cell pellet. Finally, the cell suspension was filtered through a 40 μm filter for 10×Genomics single-cell RNA sequencing.

10× Genomics single-cell RNA sequencing

SVF cells suspension isolated from young and aged group were loaded into Chromium microfluidic 3'chips barcoded with a 10× Chromium Controller (10X Genomics). RNA from the barcoded cells was reverse-transcribed, and libraries were constructed with reagents from a Chromium Single Cell 3' v3 reagent kit (10X Genomics) according to the manufacturer's instructions. Sequencing was performed by Illumina NovaSeq 6000 platform (Novogene, China).

Single-cell RNA sequencing (scRNA-seq) data processing

The Cell Ranger toolkit (version 4.0.0) provided by 10x Genomics was applied to align reads and generate the gene-cell unique molecular identifier (UMI) matrix using the mouse reference genome mm10. We applied Doublet Detection (https://github.com/JonathanShor/DoubletDetection), Scrublet [37] and DoubletFinder [38] to identify and remove potential doublets. Doublets reported by at least two tools were filtered. Then, we selected cells according to the following criteria: cells with <40,000 UMI counts; > 500 genes and <5,000 genes; and <10% UMIs derived from the mitochondrial genome. After quality control, we obtained 30,887 high-quality cells.

Unsupervised clustering and annotation of cell types

Basic processing and visualization of scRNA-seq data were performed with the Seurat package [39, 40] (version 4.0.0) in R (version 4.1.0). Firstly, the gene expression matrices were normalized to the total UMI counts per cell, multiplied by the scale factor (10,000), and then natural-log transformed. The top 2,000 highly variable genes were selected with the FindVariableFeatures function in Seurat. The obtained gene expression matrix was scaled and subjected to principal component analysis. The first 20 principal components were used for clustering analysis with suitable resolution and visualization using the uniform manifold approximation and projection (UMAP) algorithm. The marker genes were selected by FindAllMarkers function with default parameters. The cell types were annotated based on the known markers reported by published literature. Before the clustering analysis, Harmony (version 1.0) [41] was performed to batch effect correction. Endothelial cells were re-clustered by the same strategy to get a more detailed map.

DEG analysis and enrichment analysis

We used the FindAllMarkers or FindMarkers function to find differentially expressed genes (DEGs), with an average log-scaled fold change>0.25 and adjusted P value<0.01 (Wilcoxon rank sum test). For DEGs between different cell types, the top 200 genes were chosen to perform GO (Gene Ontology) enrichment analysis using the clusterProfiler package (version 3.14.3) [42]. For DEGs between aged and young group, the genes passing the screening threshold were counted to assess difference between groups in each cell type. The results were visualized by the ggplot2 R package (https://github.com/tidyverse/ggplot2). Gene set enrichment analysis (GSEA) was performed by https://www.bioi

nformatics.com.cn, an online platform for data analysis and visualization.

Definition of longevity score

The AddModuleScore function in the Seurat package was conducted to calculate the pro-longevity and anti-longevity score for every single cell in each cell type or each EC subcluster. Mouse longevity-associated genes were downloaded from the GenAge database (Table S1). "Pro-longevity" genes were beneficial to prolong life-span, and "anti-longevity" genes were considered to shorten life-span. Pro-longevity score minus anti-longevity score was considered as longevity score. P value was tested by two-sided Wilcoxon rank-sum tests.

Pseudotime analysis

Monocle 2 (version 2.16.0) [43] was used to analyze EC trajectories. We used the DEGs meeting the thresholds of an adjusted p value < 0.0001 and average log fold change > 0.4 between EC subclusters identified by Seurat to assign each cell a pseudotime. We then set the state in which most of the cells were from Endo_2 as the root_state argument and used orderCells to order cells in pseudotime. DDRTree was applied to reduce the dimensions, the visualization function plot_cell_trajectory was used to plot the minimum spanning tree on the cells. Branching Expression Analysis Modeling (BEAM) was used to identify branch-dependent and state-dependent genes.

Gene set score analysis

Metabolic gene sets were generated from 37 pathways composed of 921 unique metabolic genes (Table S2). A gene set of 449 genes related to cytokine-mediated signaling was extracted from the biological process (BP) components of the Gene Ontology (GO) database within the M5 collection available in the Mouse Molecular Signatures Database (MSigDB, Table S3). Age-related metabolic DEGs of each ECs subcluster were identified by FindMarkers function in metabolic genes with the thresholds of an adjusted p value < 0.05 and average log fold change > 0.25 (Table S4). Genes involved in proliferation of ECs were downloaded from Mouse Genome Informatics (MGI) database with GO ID:0001935 (Table S3). Genes involved in positive regulation of programmed cell death were downloaded from MGI database with GO ID: 0043068 (Table S3). Genes involved in EC senescence were downloaded from MGI database with GO ID: 0090398 (Table S3). The AddModuleScore function was used to calculate the gene set scores for each EC subcluster between young and aged groups.

Cytokine measurement of mouse SAT

RayBio® Mouse Cytokine Antibody Array G3 was used to evaluate the inflammatory cytokines species in mouse SAT and serum between two age groups. This technical service was completed by Raybiotech Life, Inc.

Evaluation of differentiation and stemness potency

Signaling entropy was computed using the R package SCENT [44] to order single cells by their differentiation potencies. This algorithm estimates network signaling entropy as a proxy for differentiated state, using literature curated protein-protein interaction databases to calculate a normalized signaling entropy value between zero and one. Using this approach, early differentiated cells manifest high network entropy.

Cell-cell communication analysis

Cell–cell interactions based on the expression of known ligand–receptor pairs in different cell types were inferred using CellphoneDB [45]. This tool evaluated the impact of the ligand/receptor interactions based on ligand expression in one cell type and the corresponding receptor expression in another cell type. This method permuted the change of cell type label for each cell at 1,000 times to calculate the significance of each pair. The P value was calculated using the proportion of the mean value for specific receptor–ligand pairs compared to a randomly permuted mean distribution. Then the communication results from two age groups were integrated to compare the Cell-cell communication difference.

Compass metabolic flux analysis

Metabolic activity analysis based on single-cell sequencing data was performed using the Compass algorithm (https://github.com/YosefLab/Compass) [46]. Compass is a flux balance analysis (FBA) algorithm based on Recon2. This algorithm employs constrained-based optimization to simulate metabolic fluxes, which represent the rates at which chemical reactions transform substrates into products. Based on transcriptomic expression levels, Compass calculates the activity of various metabolic reaction processes at the single-cell level and reflects their metabolic patterns. Compass scores and Wilcoxon rank sums were computed to assess the propensity and significance ($p < 0.001$) of various core metabolic reactions. Spearman correlation of Compass scores with potential target genes was calculated to evaluate the impact of genes on different metabolic activities. Part of the

results were visualized by the ggplot2 R package (https://github.com/tidyverse/ggplot2).

Real-time polymerase chain reaction (PCR)

Total RNA was extracted with Trizol and reverse-transcribed into cDNA with TaKaRa cDNA synthesis kit. The real-time PCR was performed using the Fast SYBR Green Master Kit and Light Cycler 480 system (Roche, Basel, Switzerland) according to the manufacturer's instructions. Primer sequences were listed in Table S5.

Measurement of cellular metabolism using Seahorse flux analyzer

Primary ECs and bEnd.3 cells were seeded at 20,000 cells per well on XFe24 V28 PS cell culture microplates (100882-004, Agilent) in endothelial cell medium (Sciencell 1001, ECM with 5% FBS and Endothelial Cell Growth Supplement). Five hours later, ECM was supplemented to 150 µL per well. Seahorse XF cell mitochondrial stress test kit (103015-100, Agilent), Seahorse XF glycolysis stress test kit (103020-100, Agilent) and Seahorse XF long chain fatty acid oxidation stress test kit (103672-100, Agilent) was used with a microfluorimetric Seahorse XF24 Analyzer (Agilent Technologies, Santa Clara, CA, USA) according to manufacturer's instructions. For analyzing the effects of siAplnr and Cxcl9 on ECs metabolism, seahorse XF24 extracellular flux analysis of ECs were performed after 3–4 days of respective treatments. Oxygen consumption rate (OCR) and extracellular acidification rate (ECAR) data were normalized to protein levels after lysing cells with RIPA buffer (50 mM Tris-HCl, pH 7.4, 150 mM NaCl, 1% Nonidet P-40, 0.5% sodium deoxycholate and 0.1% sodium dodecyl sulfate (SDS)) and quantified through a Pierce BCA protein assay kit (P0011, Beyotime).

RNA-seq and data analysis

Total RNA was extracted from untreated bEnd.3 and cxcl9-treated bEnd.3 samples labeled Ctrl_1, Ctrl_2 and Cxcl9_1, Cxcl9_2, Cxcl9_3, respectively, using TRIzol (Invitrogen), following the manufacturer's instructions. RNA was analyzed for quality and quantity using Agilent 2100 BioAnalyzer and the Qubit RNA assay kit (Invitrogen). High-quality RNA samples with RNA integrity number (RIN) > 7.0 and a 28 S:18 S ratio > 1.8 were used for library construction using CapitalBio Technology Inc. (Beijing, China) with the Ultra RNA Library Prep Kit for Illumina (NEB). After final libraries quantification using KAPA Library Quantification Kit (KAPA Biosystems, South Africa) and validation through reverse transcription-polymerase chain reaction (RT-qPCR) in Agilent 2100 Bio Analyzer, libraries were subjected to paired-end sequencing (150-base pair reads) on an Illumina NovaSeq sequencer (Illumina) by CapitalBio Technology Inc. (Beijing, China). GO terms and heatmaps were analyzed using an online bioinformatics tool (www.bioinformatics.com.cn) for data analysis and visualization.

Statistics analysis

In our study, a biological replicate refers to an independent sample from a distinct biological source (e.g., a different mouse or cell culture), while a technical replicate refers to repeated measurements from the same sample to assess technical variability. The data were presented as the mean ± SEM. All statistical tests were performed on average values derived from technical replicates for each biological replicate. Statistical analyses were performed using GraphPad Prism with unpaired Student's t-test. For gene set score analysis, statistical analyses were performed using Wilcoxon rank sum test. P values lower than 0.05 were considered statistically significant. *, **, *** and **** referred to $p < 0.05$, $p < 0.01$, $p < 0.001$ and $p < 0.0001$ respectively.

Results

Aging alters the microvascular network in subcutaneous adipose tissue by primarily affecting EC functions

To determine the impact of aging on the microvascular network, we compared female mice aged 3 months (young) with those older than 18 months (aged). We observed metabolic dysfunctions in aged mice, including high body weight and Lee obesity index, increased glucose levels, and impaired glucose tolerance (Fig. S1a-c). Moreover, we detected the corresponding increase in adipose tissue mass and a significant abundance of hypertrophic adipocytes in the SAT of aged mice (Fig. S1d). Considering the heterogeneous adaptations of the vascular endothelium during aging [47], we conducted single-cell RNA sequencing (scRNA-seq) of the stromal vascular fraction (SVF) obtained from mouse SAT and compared samples from four young and three aged mice. After cell filtering and batch-effect correction, 30,887 high-quality SVF cells (14055 cells from young mice and 16832 cells from aged mice) were obtained (Fig. S1e). Visualization of cell types using UMAP revealed 24 cell clusters with distinct gene expression signatures (Fig. S1f, and Table S6). Based on the expression matrix of the specific markers, 15 cell types were manually annotated (Fig. 1a-b, Fig. S1g, and Table S7). The cell type compositions were similar among the young and aged mice (Fig.S1h). We classified

4366 cells (2,265 from young mice and 2,101 from aged mice) expressing CD31 and Cldn5 as ECs.

Subsequently, we calculated the number of differentially expressed genes (DEGs,|avg_log2FC| > 0.25 and adjusted P value < 0.01) in the aged mouse SVF compared to the young counterparts (Fig. 1c and Table S8). Notably, ECs exhibited the largest number of total DEGs (307 up-regulated and 358 down-regulated genes in aged group), including shared DEGs (155 upregulated and 203 downregulated genes in the aged group; Fig. 1c, upper half) and cell-type specific upregulated DEGs (152 genes in the aged group, Fig. 1c, lower half). These findings suggest that aging more significantly affects the transcriptional state of ECs than that of other SVF cells. We conducted an integrative comparative analysis of the DEGs with longevity-associated genes from the GenAge database (Table S1). ECs, Adipose progenitor and stem cells (APCs), and T cells exhibited the most significant decrease in the longevity score in aged mouse SVF (Fig. 1d), which emphasized the leading role of ECs during SVF aging.

We explored the aging-associated changes in the characteristics of the aged microvascular endothelium via bulk adipose tissue clearing and light-sheet immunofluorescence imaging assay. We detected a distorted morphology and a significant (> 50%) reduction in the density of the vascular network in the SAT of aged mice (Fig. 1e). Consistently, primary ECs isolated from aged mouse SAT exhibited reduced angiogenic potential, as evidenced by a lower total branching length and the number of meshes revealed by the tube-formation assays (Fig. 1f). In addition, we observed a significant increase in the number of senescent cells in primary ECs cultures derived from aged mice, as evidenced by positive staining for SA-β-gal (Fig. 1g). These findings collectively highlight the pivotal role of EC dysfunction in age-related alterations in SAT microvascular networks.

Venular ECs exhibit the most notable pseudotemporal state transition during aging

Next, we assessed the features of microvascular EC subpopulations during aging. Based on unsupervised clustering analysis, we identified seven subpopulations of ECs, labeled Endo_0 to Endo_6 (Fig. 2a). Endo_0 and Endo_1 collectively comprised > 50% of the ECs population (Fig. 2b). Based on the distinctive transcriptional profiles of each ECs subcluster (Table S9) and previous reports, Endo_0 and Endo_1 were identified as capillary ECs co-expressing the universal capillary EC markers Car4 and Rgcc (Fig. 2c, Fig. S2a). Endo_3 cells were identified as venular ECs and characterized by the expression of atypical chemokine receptor 1 (Ackr1), Selp28, Lrg1, and Vcam1 (Fig. 2c, Fig. S2a). Endo_4 cells are recognized as arteriolar ECs that express high levels of Fbln5, Sema3g, Hey1, and Efnb2 (Fig. 2c, Fig. S2a).

Endo_2, 5, and 6 were considered relatively independent sub-clusters in the two-dimensional UMAP plot (Fig. 2c). Endo_2 emerged as a novel progenitor EC subcluster located in the root state in the pseudotemporal trajectory panel and exhibited the highest stemness entropy (Fig. 2d, Fig. S2b). Moreover, Endo_2 expressed markers specific to multiple cell types, including pericytes (Rgs5, kcnj8, Abcc9, and Pdgfrb) and smooth muscle cells (Acta2 and Tagln) (Table S9, Fig. S2a), which enriched in muscle tissue development and contraction (Fig. 2c). According to a recent report, Endo_5 cells were defined as prevenular capillary ECs based on high expression of the cytoskeleton and extracellular matrix genes (Gsn, Tmsb10, and Col3a1) and genes involved in ribosome biogenesis (Rpls); Endo_6 was classified as post-capillary venular ECs based on the expression of the postcapillary venular marker Lrg1 [48] (Fig. 2c, Fig. S2a).

To uncover the differentiation states of ECs subtypes in aging progression, we used the Monocle2 package to construct single-cell trajectories and generated a spanning tree starting from progenitor Endo_2 (state 5), which branched into two separate paths, leading to states 1 and 6 (Fig. 2d). The young and aged ECs displayed a reciprocal shift in the proportions corresponding to the states 1 and 6 (Fig. 2e-f, Fig. S2c). Specifically, most young ECs resided in state 1 (41.03%) rather than in state 6 (12.18%), whereas state 1 ECs dramatically decreased to < 6% in aged mice and state 6 being the predominant state (46.38%). This transition signifies a shift in ECs phenotype, highlighting state 1 as indicative of youthful state and state 6 as a terminal state related to aging.

A similar transition was observed across all EC subtypes in aged mice, except for progenitor ECs (Endo_2), which exhibited continuous residence in state 5 (Fig. 2g, Fig. S2d). Venular ECs (Endo_3) showed the most pronounced and significant decline in state 1 with aging (86% in young mice vs. < 20% in aged mice). Correspondingly, the proportion of venular ECs in state 6 increased nearly 30-fold with age. These findings suggest that venular ECs comprise the leading subpopulation of ECs in age-related pseudotemporal state transition.

Aging induces a selective reduction in the proportion of venular ECs within the ECs population

To further explore the molecular characteristics of aged venular ECs, we explored their transcriptional changes by analyzing scRNA-seq data. We identified 404 significant DEGs, including 218 upregulated and 186 downregulated ones (P value < 0.01 and |log2 FC| > 0.25, Table S10). Gene ontology

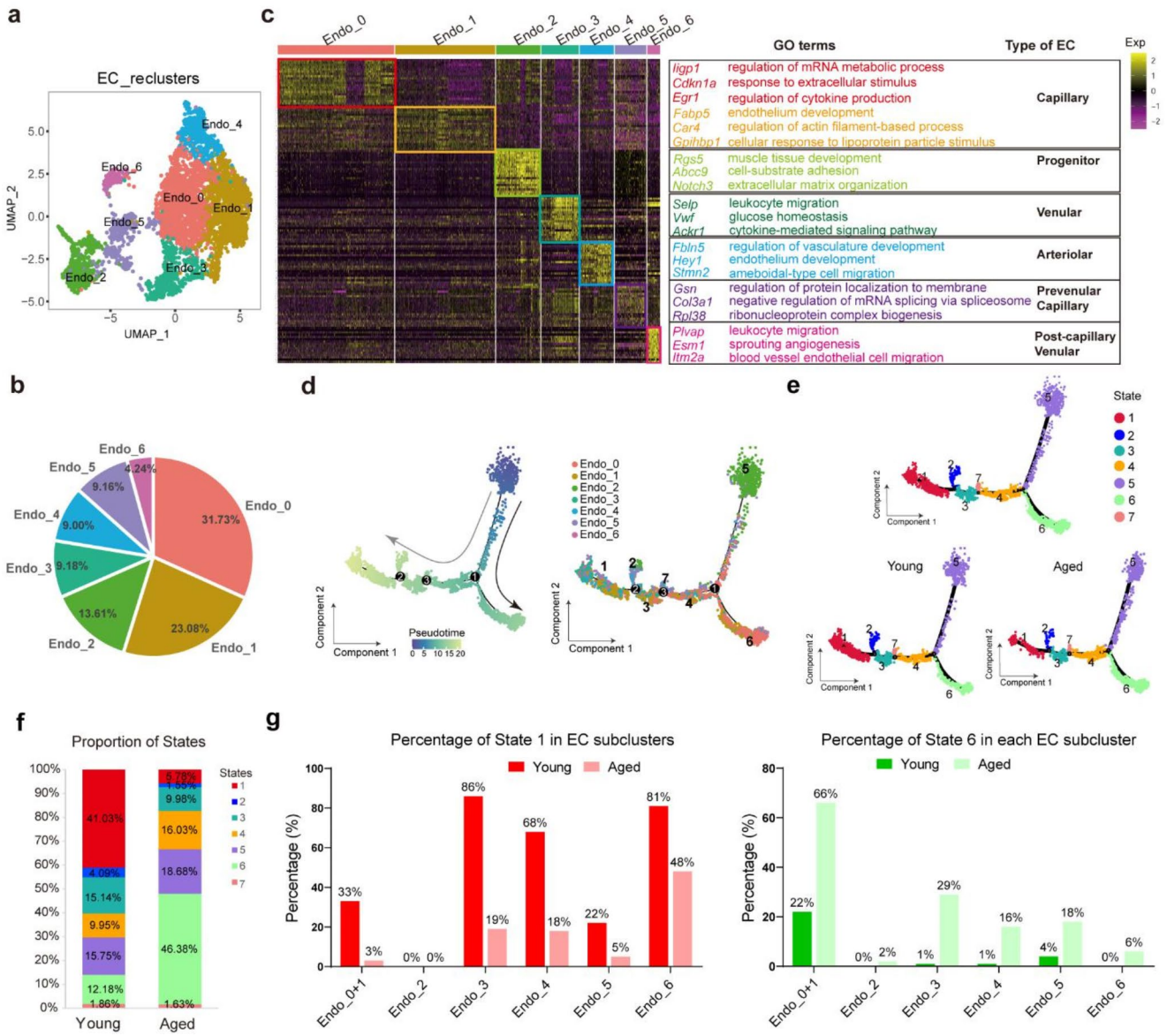

Fig. 2 Venular ECs show the most notable pseudotemporal state transition during aging. (**a**) UMAP clustering of ECs in mouse SAT. (**b**) The cell percentage of each EC subpopulation in the integrated aged ($n=3$) and young ($n=4$) SVF samples. (**c**) Scaled expression levels of highly expressed genes in each EC subpopulations. The color key from purple to yellow represente low to high gene expression levels. Subpopulation-specific representative genes and enriched GO terms are labelled on the right side by color. (**d**) Pseudotemporal trajectory analysis of EC subpopulations. Pseudotime ordering of ECs subpopulations is depicted by pseudotime (left) and subpopulation (right), the color key ranging from blue to yellow represents 0 to 20 by pseudotime. (**e**) UMAP plot of pseudotemporal trajectory analysis of young and aged ECs along with discriminative dimensionality reduction via learning a tree (DDRTree) depicts seven states. (**f**) The column chart shows the percentages of ECs in each of the seven states in young and aged mice. (**g**) The percentage of cells in state 1 (upper) and state 6 (lower) in each ECs subpopulation from young ($n=4$) and aged ($n=3$) mice

(GO) enrichment analysis revealed that up-regulated DEGs were most significantly involved in the positive regulation of programmed cell death, protein refolding, negative regulation of blood vessel morphogenesis, and positive regulation of cytokine production, indicating increased apoptosis and inflammation in venular ECs under aging stress (Fig. 3a). Contrastingly, the downregulated DEGs were enriched for cytoplasmic translation, extracellular matrix organization, glucose homeostasis, and vascular development. Altered biological processes are inextricably linked to impaired vascular function and growth. Next, the analysis of the proportion of each ECs subpopulation revealed a decrease in venular ECs (from 10.82 to 6.98%) and an increase in capillary ECs (from 49.44 to 61.97%) within the aged EC population (Fig. 3b). Ackr1, known as the Duffy antigen receptor for chemokines (DARC), is specifically expressed

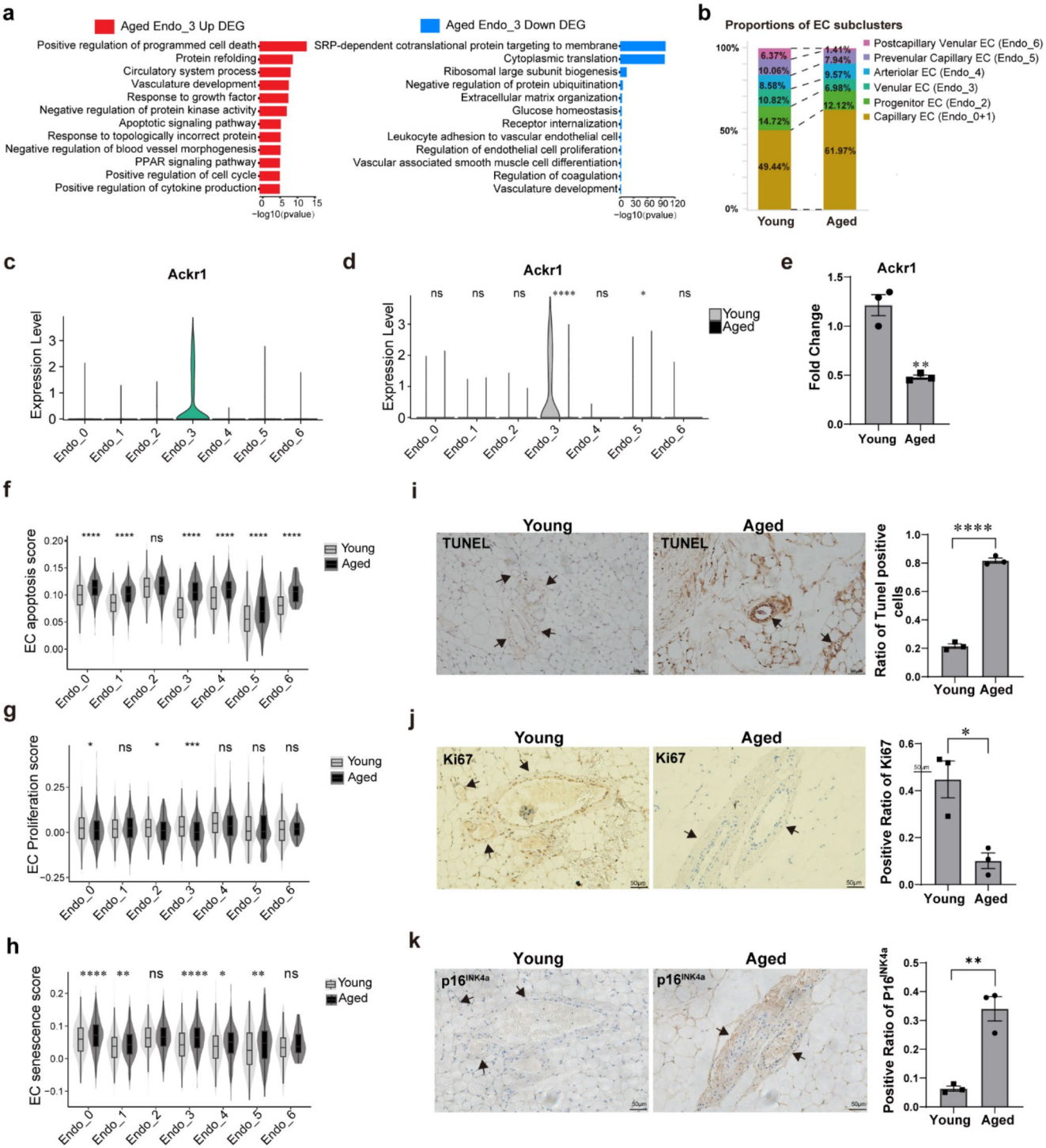

Fig. 3 Aging induces a selective reduction in the proportion of venular ECs within the ECs population. (**a**) GO enrichment analysis of up-regulated and down-regulated DEGs in aged Endo_3. (**b**) The proportion of each EC subpopulation in young and aged mice. (**c-d**) Expression of Ackr1 in each EC subpopulation (**c**) and transcriptional changes of Ackr1 in each EC subpopulation (**d**) by scRNA-seq analysis. (**e**) Real-time qPCR analysis revealed differential level (fold change) of Ackr1 transcription in aged ECs compared to young ECs. Data are presented as mean ± SEM, $^{**}P<0.01$ based on Student's t test, $n=2$ technical replicates for 3 biological replicates of each group. (**f-h**) Comparison of the apoptosis (**f**), proliferation (**g**), and cellular senescence (**h**) signaling scores of individual cells in each EC subpopulation between young and aged mice. ns, no significance; * $P<0.05$, ** $P<0.01$, *** $P<0.001$, **** $P<0.0001$ based on two-sided Wilcoxon rank-sum test. (**i-k**) Histological identification of apoptosis, proliferation, and cellular senescence in vascular ECs. Apoptosis of vascular ECs is evaluated using TUNEL assay (**i**), proliferation is assessed by Ki67 immunohistochemistry (**j**), and senescence is determined through $p16^{INK4a}$ immunohistochemistry (**k**). The number of positive cells is determined by averaging the counts from three randomly selected microscopic fields on each section ($n=3$) using high-power magnification. Data are presented as mean ± SEM, * $P<0.05$, ** $P<0.01$, and $^{****}P<0.0001$ based on Student's t test. Scale bar, 50 μm

in venular ECs [49] and plays a crucial role in leukocyte trafficking and extravasation into peripheral tissues [48, 50]. Consistently, our scRNA-seq data revealed that Ackr1 primarily expressed in the venular EC subtype (Fig. 3c), and its expression was significantly downregulated in venular ECs subtypes in aged mice SAT (Fig. 3d); this outcome was confirmed using real-time PCR (Fig. 3e).

We then performed Seurat's AddModuleScore function to evaluate the apoptosis, senescence and proliferative scores of each ECs subpopulation. A significant increase in apoptosis levels across all aged EC subpopulations was identified, except for progenitor (Endo_2) ECs (Fig. 3f). Proliferation scores were significantly decreased in three EC subclusters, with venular ECs showing the most pronounced decrease (Fig. 3g). Additionally, the senescence score was significantly increased in most aged EC subpopulations, particularly capillary (Endo_0) and venular ECs (Fig. 3h). To further explore why aged venular ECs exhibited the most significant reduction in proliferation score, we analyzed the transcriptional changes of genes involved in regulation of EC proliferation in all EC subtypes. Thbs1 [51] and Rgcc [52], two negative regulators of EC proliferation, were significantly upregulated in venular EC subtypes; the change was either distinct (for Thbs1) or exclusive (for Rgcc) (Fig. S2e-f). These findings indicate that the decreased proliferation of venular ECs potentially contributes to an age-related reduction in the proportion of venular ECs within the EC population. TUNEL staining and immunohistochemistry staining on sections of mice SAT showed that vascular ECs in aged mice SAT exhibited a higher ratio of TUNEL-positive and $p16^{INK4a}$-positive cells, as well as lower expression of the proliferation marker Ki67 (Fig. 3i–k).

Reduced oxidative phosphorylation and enhanced cytokine signaling are key features of all aged EC subtypes

To elucidate the shared molecular characteristics and mechanism linking the states shifting across most of the EC subtypes along the aging process, we compare gene expression kinetics across trajectories to state 1 and 6, using branched expression analysis modeling (BEAM). Gene modules with similar lineage-dependent expression patterns were hierarchically clustered for visualization (Fig. 4a and Table S11). The 1011 state 6-dependent genes (upregulated in state 6) were notably enriched in processes associated with the positive regulation of programmed cell death, fatty acid metabolism, negative regulation of vascular development, and inflammatory response. Conversely, 1075 state 1-dependent genes that were downregulated in state 6 were enriched in protein synthesis, oxidative phosphorylation, ATP metabolic processes, mitochondrial function, and extracellular matrix (ECM) organization-related processes.

Fig. 4 Reduced oxidative phosphorylation and enhanced cytokine signaling are key features of all aged ECs subtypes. (**a**) Heatmap of the branched expression analysis modeling (BEAM) revealing significant changes through progression across the trajectory from state 5 (root state) to state 1 and 6. Each row indicates the standardized kinetic curves of a gene. (**b**) Venn diagram depicting the number of overlapping DEGs shared between aged ECs and the pseudotemporal states 1 or 6 (State6/Aged EC up-regulated DEGs, state 1/Aged EC down-regulated DEGs). (**c**) Gene Set Enrichment Analysis (GSEA) of the hallmark pathways of upregulated (upper) and downregulated (lower) genes in ECs from aged mice. (**d**) Comparison of the gene set score (left: cytokine-mediated signaling pathway, right: oxidative phosphorylation pathway) of each single cell in each EC subpopulation between young and aged mice. * $P<0.05$, ** $P<0.01$, and **** $P<0.0001$ by two-sided Wilcoxon rank-sum tests. (**e**) Compass-score differential activity test between ECs from young and aged mice. x-axis, Cohen's d; y-axis, $-\log_{10}$(Wilcoxon-adjusted P value). $-\log_{10}$(Wilcoxon-adjusted P value) > 1.0 is considered as significant. (**f-g**) Cellular metabolism analysis of primary ECs harvested from young and aged mice SAT using Seahorse XF Cell Mito Stress Assay kit (**f**) and Glycolysis Stress Assay kit (**g**), Data are presented as mean ± SEM, *$P<0.05$ by Student's t test. For both the young and aged groups, two technical replicates are conducted for each of the three biological replicates ($n = 3$)

Furthermore, > 90% of the up-regulated and > 80% of the down-regulated DEGs in the aged bulk EC population were enrolled in state 6-specific trajectories (Fig. 4b). GSEA suggested TNF-α signaling via NFκB to be the most significantly upregulated pathway and oxidative phosphorylation as the most downregulated pathway (Fig. 4c). Consistently, we observed a significant increase in the gene set score for cytokine signaling and a decrease in the score for oxidative phosphorylation across all aged ECs subpopulations (Fig. 4d). These results indicate that enhanced cytokine signaling and suppressed oxidative phosphorylation are key characteristics of aged ECs.

Subsequently, we analyzed the metabolic state of the cells using the Compass algorithm. The Compass scoring system evaluates individual metabolic reaction or enzyme based on the entire metabolic transcriptome, rather than just the mRNA levels of the enzymes involved. The Compass scores of all reactions/enzymes in the tricarboxylic acid (TCA) cycle (the major common pathway for the oxidation of carbohydrates, lipids, and some amino acids, which results in ATP production via oxidative phosphorylation) were significantly decreased in aged ECs (Fig. 4e). Particularly, isocitrate dehydrogenase (IDH), a key enzyme in the TCA cycle that catalyzes the irreversible conversion of isocitrate to alpha-ketoglutarate, exhibited the most significant decrease. In addition, most of the enzymes/reactions involved in glycolysis were downregulated in aged ECs. However, the changes in reactions/enzymes involved in amino acid and fatty acid metabolism were diverse, including both increases and decreases in aged ECs. To validate the Compass prediction, we assessed the mitochondrial function

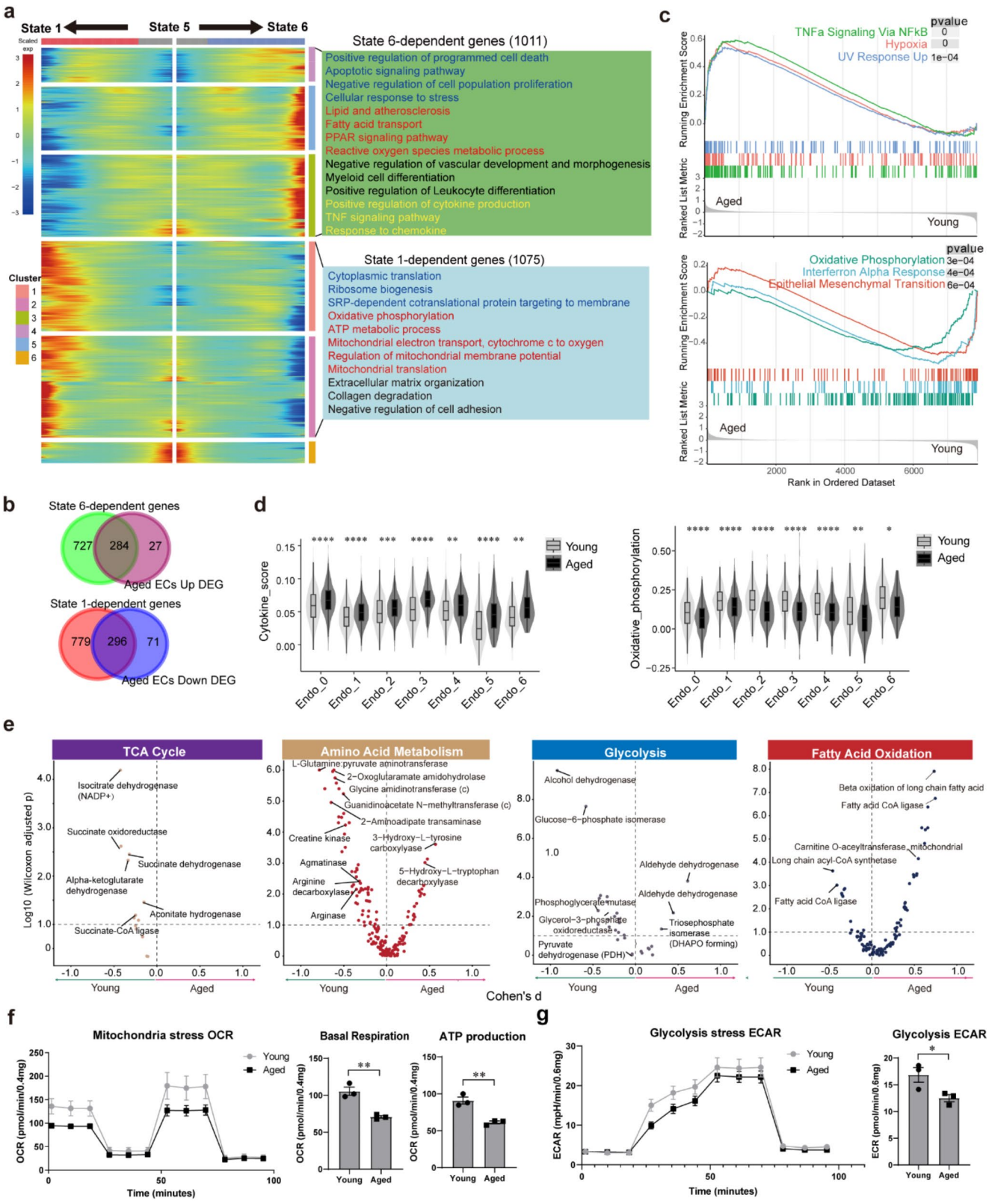

and glycolysis of ECs using seahorse assays. Primary ECs acquired from the SAT of aged mice showed diminished basal respiration and mitochondrial ATP production, which was consistent with the predicted lower compass score of enzymes/reactions in the TCA cycle (Fig. 4f). Similarly, aged ECs exhibited a reduced ECAR that aligned with the

Compass prediction (Fig. 4g). Therefore, both Compass and metabolomics data reflected that the suppression of oxidative phosphorylation is the key metabolic trait present in aged microvascular ECs.

Enhanced expression of endothelial Cxcl9 highly correlates with metabolic alterations in aged ECs

We investigated whether the metabolic alterations in aged ECs were correlated with enhanced cytokine-mediated signaling. First, the scRNA-seq data of ECs populations revealed 13 cytokines (10 upregulated and 3 downregulated) that exhibited significantly differential expressions (P value < 0.01 and |log2 FC| > 0.25) in aged ECs (Fig. 5a). Based on the changing patterns, these cytokines could be categorized into groups. For instance, the expressions of *Ccl5*, *Ccl6*, *Ccl8*, *Ccl9*, *Cxcl2*, and *Pf4* were upregulated across all aged ECs subpopulations, with the most significant increase observed in aged pre-venular capillary ECs (Endo_5). In contrast, enhanced expressions of *Cxcl1* and *Gdf15* were predominantly detected in aged progenitor ECs (Endo_2). Conversely, *Cxcl12*, *Tnfsf10*, and *Tgfb2* were suppressed in most ECs subpopulations, with the most notable decrease in arteriolar ECs (Endo_4). However, *Cxcl9* and *Inhbb*, two separate cytokines, were primarily increased in venular ECs (Endo_3) and post-capillary venular ECs (Endo_6), respectively.

Next, using Spearman correlation analysis of Compass scores with the identified 13 cytokines, we defined 309 significant metabolic reactions/enzymes (|cor_r| > 0.3, BH-adjusted $P < 0.05$) that were correlated or anti-correlated with at least one cytokine (Fig. 5b and Table S12). Similar to the changing patterns of these cytokines, the correlations between cytokines and metabolic enzymes can be categorized into groups. Interestingly, *Cxcl9* was upregulated in aged ECs and showed dual effects on EC metabolism, exhibiting the most distinct negative correlation with isocitrate dehydrogenase (IDH), an enzyme predicted via Compass to be substantially downregulated in the TCA cycle of aged ECs. In contrast, cxcl9 showed the strongest positive correlation with multiple enzymes involved in fatty acid metabolism (Fig. 5b). This was consistent with our previous finding that terminal aging state 6-dependent genes are functionally enriched in fatty acid metabolism (Fig. 4a). Overall, these data indicate that *Cxcl9* is a potential cytokine correlated with metabolic alterations in aged ECs.

To validate the expression pattern of Cxcl9 in ECs after aging, we first analyzed scRNA-seq data. The analysis revealed significant increases in both Cxcl9 expression levels and the proportion of Cxcl9-positive cells across most aged EC subtypes, especially venular ECs (Endo_3) (Fig. 5c, Fig. S3). Among all SVF cell types, ECs exclusively expressed Cxcl9 and it was significantly elevated in the bulk population of aged ECs (Fig. 5d). Histoimmunofluorescent staining of Cxcl9 revealed that the expression of Cxcl9 was significantly increased in aged CD31+ ECs (Fig. 5e-f).

Furthermore, the cytokine antibody array was used to detect the composition and levels of cytokines in mouse SAT lysates. A total of 38 differentially expressed cytokines (Log2FC > 1.2 and adjusted P value < 0.05) were identified in the SAT lysate between aged and young mice, including 33 upregulated and 5 downregulated cytokines (Fig. 5g and Table S13). The most upregulated cytokines in the aged group were well-documented senescence-associated secretory phenotype (SASP) proteins, substantiating local inflammation in the aged mouse SAT. Notably, the level of Cxcl9 was significantly increased in aged mouse SAT lysates. Accumulated evidence suggests that Cxcl9 expression is induced by IFN-γ [53]. Consistently, our cytokine array revealed that IFN-γ levels significantly increased in the aged mice SAT. Therefore, we speculated that aging potentially induces the expression of Cxcl9 in ECs through a paracrine effect by increasing the levels of IFN-γ in the adipose tissue.

Moreover, Cxcl9 signals through the CXCR3 receptor, primarily expressed in immune cells. Based on our scRNA-seq data, we detected that Cxcr3 was predominantly expressed in T cells; upon aging, its expression was significantly increased in T cells and neutrophils (Fig. S4a). We used CellphoneDB to explore the crosstalk between endothelial Cxcl9 and Cxcr3 expressed in immune cells (Fig. S4b). In aged SVF, this crosstalk between ECs and T cells intensifies. Moreover, additional Cxcl9-cxcr3 crosstalk was detected between ECs and neutrophils (EC/neutrophils), as well as between ECs and B cells (EC/B). These findings suggest that elevated endothelial Cxcl9 strengthens its communication with immune T cells, B cells, and neutrophils, contributing to the pro-inflammatory microenvironment of the aged mouse SAT.

Cxcl9 impairs the energy metabolism and angiogenesis of microvascular ECs

To further explore the role of Cxcl9 in microvascular EC aging, we treated an immortalized mouse brain microvascular EC line (bEnd.3) with 100μM Cxcl9 in vitro and performed bulk RNA-sequencing (RNA-seq) transcriptome analysis. GSEA of Cxcl9-treated ECs revealed the upregulation of genes involved in biological processes, including the immune response, fatty acid metabolism, and cytokine production, as well as downregulation of genes involved in ECs proliferation, oxidative phosphorylation, and glucose metabolism (Fig. 6a). This profile is comparable to the previously reported characteristics of aged ECs. Furthermore,

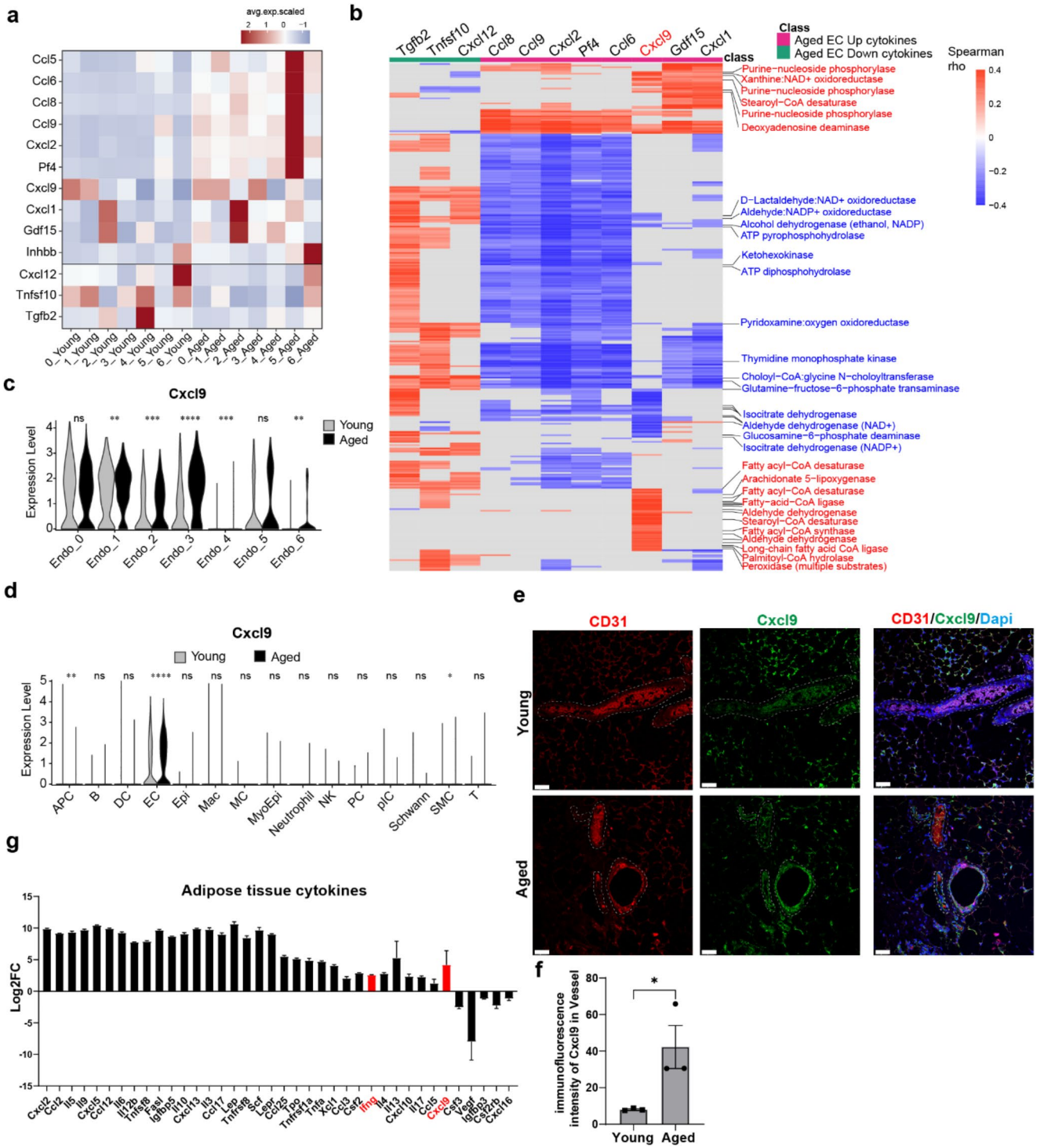

Fig. 5 Up-regulation of Cxcl9 induced by aging is highly correlated with metabolic alterations of aged ECs. (**a**) Heatmap of the 13 differentially expressed cytokines (P value < 0.01 and|log2 FC| >0.25) in EC subpopulations compared between young ($n = 3$) and aged ($n = 3$) mice. (**b**) Spearman correlation of Compass scores with the expression of upregulated or downregulated cytokine genes in aged mice SATs. Non-significant correlations (BH-adjusted $p \geq 0.1$) are indicated in grey. Metabolic reactions are listed in rows, representing core pathways, each significantly correlated or anti-correlated with at least one gene. (**c-d**) Expression of Cxcl9 in ECs subpopulations (**c**) and SVF cell types (**d**) analyzed by scRNA-seq. ns, no significant. $^{*}P < 0.05$, $^{**}P < 0.01$ and $^{****}P < 0.0001$ by two-sided Wilcoxon rank-sum tests. (**e**) Histo-immunofluorescent staining of Cxcl9 and CD31 in mice SAT, with vascular tissue outlined by gray dashed lines. Scale bar, 50 μm. (**f**) The intensity of Cxcl9 fluorescence signals in the vascular are quantified using LAS-X software. The images are captured from three randomly selected confocal microscopic fields on each section ($n = 3$) using high-power magnification. Data are presented as mean ± SEM; $^{*}P < 0.05$ based on Student's t test. (**g**) The variable levels (fold changes) of differentially expressed cytokines in SAT lysate of aged mice. Cytokine levels of adipose tissues are measured in 3 young and 3 aged mice. Data are presented as mean ± SEM

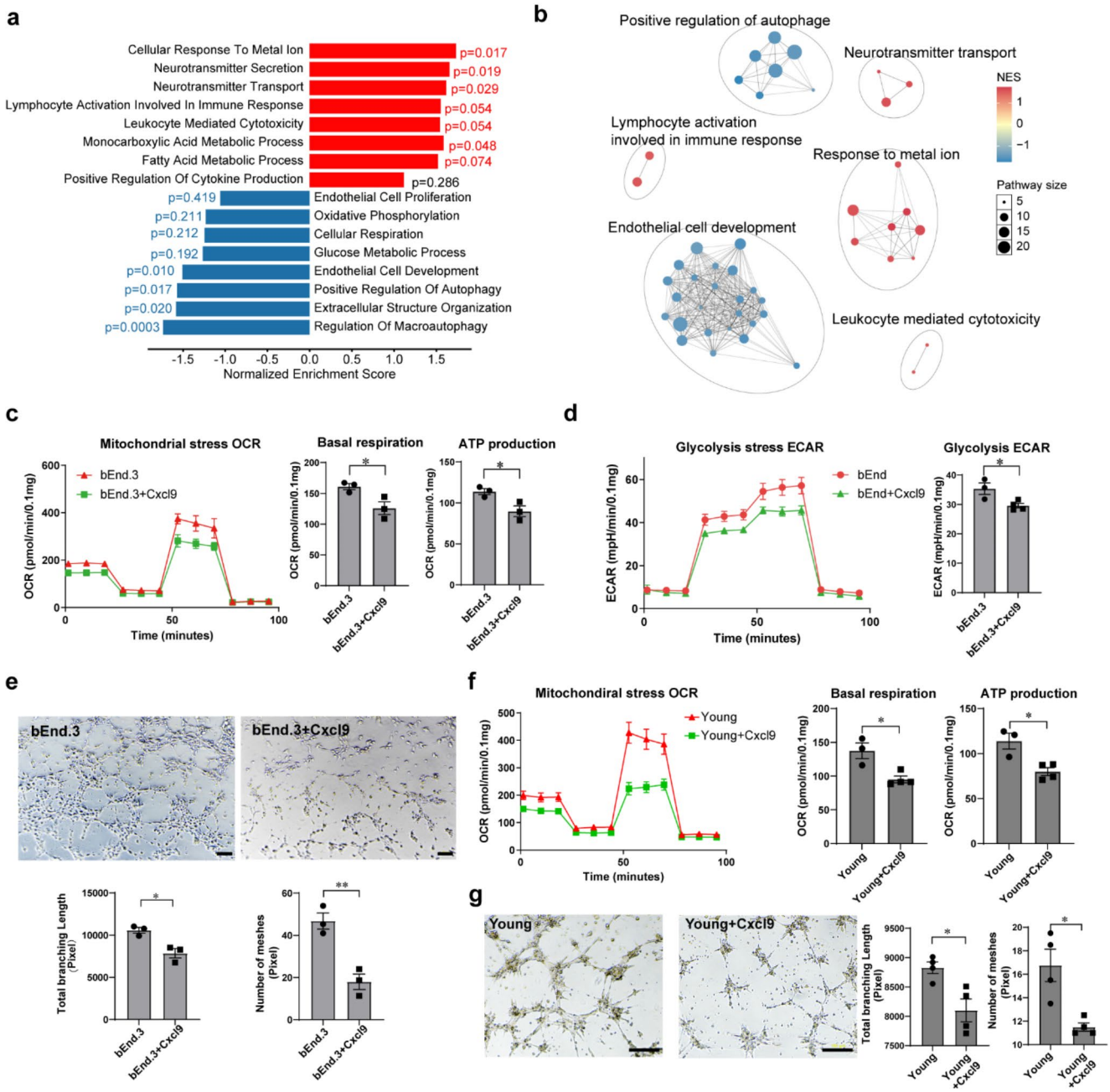

Fig. 6 Cxcl9 impairs the energy metabolism and angiogenesis of microvascular ECs. (**a**) GSEA comparing bEnd.3 and Cxcl9-treated bEnd.3. (**b**) GSEA gene set network analysis comparing bEnd.3 and Cxcl9-treated bEnd.3. (**c-d**) The effect of Cxcl9 on cellular metabolism of bEnd.3 cells analyzed using Seahorse XF Cell Mito Stress Assay **(c)** and Glycolysis Stress Assay kits (**d**). Data are presented as mean ± SEM, $*P<0.05$ by Student's t test, $n=3$ biological replicates for each group for (**c**), $n=3$ biological replicates for young group and $n=4$ biological replicates for aged group for (**d**). (**e**) Tube formation assay conducted using Cxcl9-treated and untreated bEnd.3 ECs. The total branching length and the number of meshes were measured and compared using Angiogenesis Analyzer plugin in imageJ. Three microscope fields randomly selected from each well ($n=3$ per group) are assessed. Data are presented as mean ± SEM; $*P<0.05$ and $**P<0.01$ based on Student's t test. (**f**) The effect of Cxcl9 on mitochondrial metabolism in the primary SAT ECs of young mice analyzed with the Seahorse XF Cell Mito Stress Assay. There are 3 biological replicates for the control group and 4 biological replicates for the Cxcl9 administration group. Data are presented as mean ± SEM; $*P<0.05$ based on Student's t test. (**g**) Tube formation assay conducted using Cxcl9-treated and untreated primary ECs from the SAT of young mice. Data are analyzed using Angiogenesis Analyzer plugin in imageJ. Three microscope fields randomly selected from each well ($n=4$ per group) are assessed. Data are presented as mean ± SEM; $*P<0.05$ based on Student's t test. Scale bar: 100 μm

we performed GSEA gene set network analysis using the R package *aPEAR* and found that genes downregulated in pathways related to EC development formed the largest cluster (Fig. 6b). This finding underscores the deteriorating effect of Cxcl9 on energy metabolism and vascular growth of ECs.

We validated the impact of Cxcl9 on EC function through Seahorse XF energy metabolism assays in bEnd.3 ECs. Treatment with Cxcl9 for three days induced a significant reduction in basal respiratory capacity and ATP production in bEnd.3 ECs than in the control counterparts (Fig. 6c), as well as a decrease in glycolytic capacity (Fig. 6d). Cxcl9-treated bEnd.3 ECs exhibited a decreased ability to form tubular network structures (Fig. 6e), which was consistent with the suppression of pathways associated with EC development, as indicated by GSEA (Fig. 6b). Moreover, treatment with Cxcl9 also significantly decreased the basal respiration, ATP production, and angiogenic capacity of ECs isolated from young mice SAT (Fig. 6f-g). These results suggested that Cxcl9 has a broad impact on ECs function across different tissues.

Cxcl9-mediated suppression of Aplnr contributes to the age-related EC dysfunction

We further investigated the molecular mechanisms underlying EC dysfunction triggered by enhanced Cxcl9 signaling through a comparative analysis of the transcriptional profiles in untreated and Cxcl9-treated bEnd.3 cells. We observed 288-up-regulated DEGs and 444 downregulated DEGs ($P<0.05$, |log2 FC| >0.15; Table S14). Considering that reduced energy metabolism and angiogenesis are the validated shared characteristics of Cxcl9-treated bEnd.3 ECs and ECs derived from aged mouse SAT, we focused on the downregulated DEGs in Cxcl9-treated bEnd.3 cells. GO analysis revealed the most significant enrichment of these DEGs in G protein-coupled receptor signaling pathways (Fig. 7a). Seven genes were assigned to this biological process (Fig. 7b). Notably, Aplnr, also known as APJ/apelin receptor, is a G protein-coupled receptor that mainly present in vascular ECs, smooth muscle cells, and cardiomyocytes [54]; it was the sole gene found among the downregulated DEGs in ECs of aged mice (Fig. 7c). Next, Aplnr expression showed a significant decrease in bEnd.3 cells treated with either Cxcl9 or the Cxcl9-downstream secondary messenger cAMP, as determined by real-time PCR analysis (Fig. 7d). Consistently, Aplnr expression in ECs isolated from aged mouse SAT was significantly reduced (Fig. 7e).

Next, our scRNA-seq data revealed that Aplnr expression was specifically confined to ECs in mice SVF and exhibited a pronounced age-induced decrease in the entire EC population and across all EC subtypes (Fig. 7f). Moreover, pseudo-time trajectory analysis revealed contrasting expression patterns of Cxcl9 and Aplnr during age-related state transitions (Fig. 7g). Cxcl9 expression consistently increased from state 5 to state 6 and decreased along the path to state 1, whereas Aplnr expression exhibited a contrasting trend. To determine whether the inhibition of Aplnr could recapitulate the effects of Cxcl9 on energy metabolism and angiogenesis in ECs, we performed seahorse energy metabolism assays and tube formation analysis following silencing of Aplnr using siRNA. Real-time PCR results validated the significant downregulation of Aplnr mRNA levels in ECs treated with SiAplnr (Fig. 7h). The basal respiration, ATP production, glycolytic capacity and tube formation abilities of bEnd.3 cells were significantly reduced after four days of treatment with SiAplnr (Fig. 7i-k). Collectively, these data suggest that the suppression of Aplnr potentially contributes to Cxcl9-mediated EC dysfunction in aged ECs.

Finally, to explore the possible transcriptional mechanisms linking increased Cxcl9 to reduced Aplnr, we reviewed our RNA-seq data and identified eight transcription factors (TFs), significantly (|Log2FC|>0.25, $P<0.05$) downregulated in Cxcl9-treated bEnd.3 cells, and three TFs that were significantly up-regulated (Fig. S5a). We used JASPAR to predict transcription factor-binding sites within the promoter region of Aplnr. With the track score > 500 (P-value $<10^{-5}$), Foxc1 represented one of the 11 significantly altered TFs with binding site located in the Aplnr promoter (Fig. S5b). After scanning, eight binding sites of Foxc1 were predicted in the Aplnr promoter region (Fig. S5c). Moreover, we found that Foxc1 was highly expressed in the Endo_3 venular ECs, which significantly downregulated with aging (Fig. S5d). These findings suggest that Cxcl9 reduces Aplnr expression through the suppression of Foxc1 in aged ECs.

Next, we explored whether these age-related transcriptional alterations affected the crosstalk between ECs and other cells within the SVF of mice using CellphoneDB. Ligand-receptor pairs with fold changes in communication score (aged vs. young) over 1.5 and P values < 0.05 were selected and visualized as dot plots (Fig. S5e). Crosstalk between ECs and APCs through Aplnr-Apln pairing was suppressed most significantly. These findings suggest that Cxcl9-induced suppression of Aplnr in ECs possibly weakens the communication between APC and ECs. Further experiments are needed to explore whether these changes contribute to the functional decline of the aged microvasculature in adipose tissue.

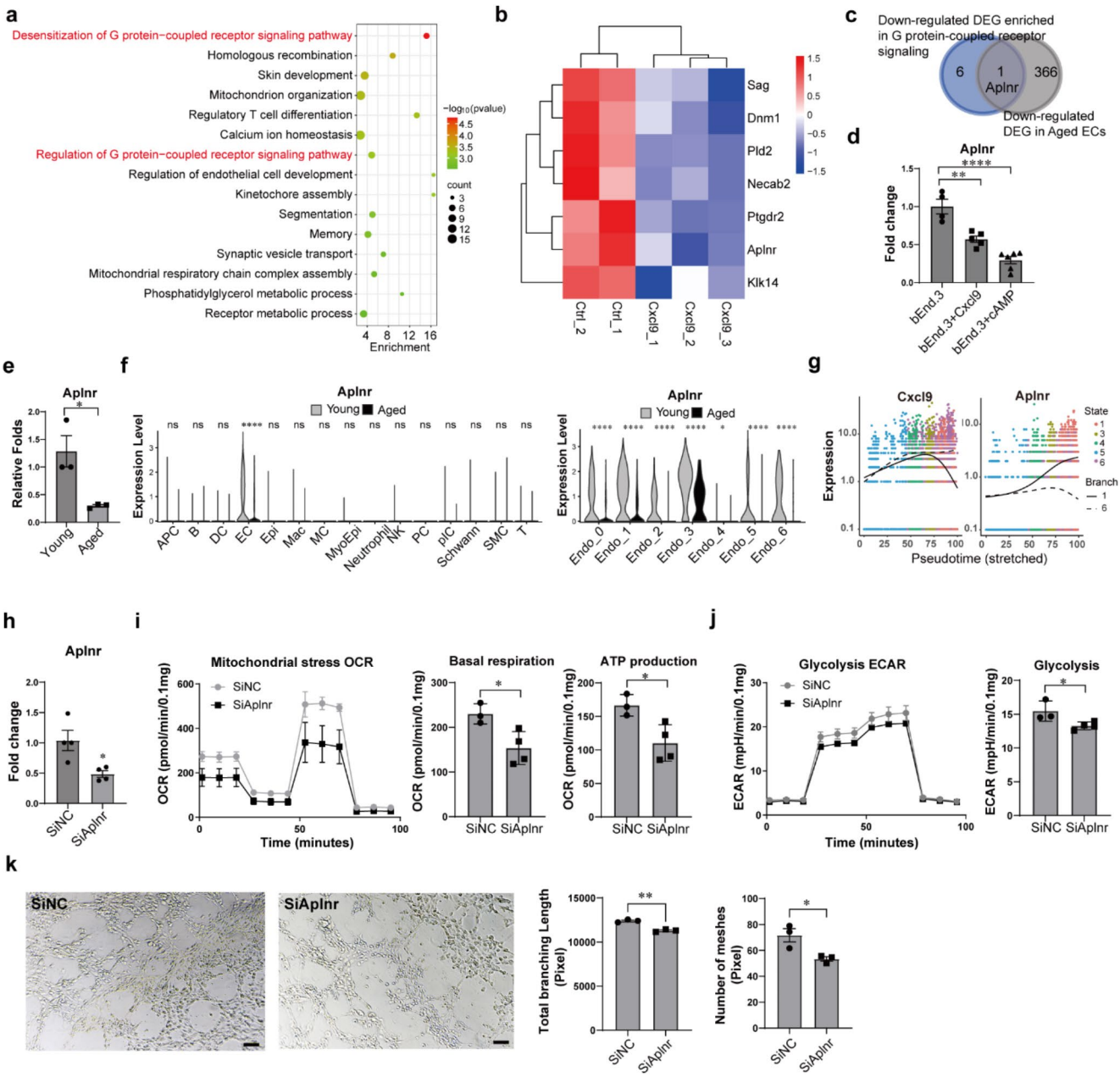

Fig. 7 Cxcl9-mediated suppression of Aplnr contributes to age-related EC dysfunction. (**a**) Gene Ontology (GO) enrichment analysis of down-regulated DEGs in Cxcl9-treated bEnd.3 cells. (**b**) Heatmap showing expressions of genes related to the regulation of G-protein-coupled receptor signaling in Cxcl9-treated and untreated ECs. (**c**) Venn diagram depicting Aplnr as the solo down-regulated DEG shared between primary ECs from aged mice and cxcl9-treated bEnd.3 cells. (**d**) Real-time qPCR assays assessed the effects of cxcl9 and cAMP on the expression of Aplnr in bEnd.3 cells. Data are presented as mean ± SEM, $^{**}P < 0.01$, $^{***}P < 0.0001$ based on Student's t test; $n = 4$ biological replicates for control group, $n = 5$ for Cxcl9 treatment group and $n = 6$ for the cAMP treatment group. (**e**) Variations in (fold changes) Aplnr expression in primary ECs isolated from aged mice in comparison to young mice. Data are presented as mean ± SEM; $^{*}P < 0.05$ based on Student's t test; three biological replicates were conducted for each group. (**f**) Expression of Aplnr in SVF cell types and ECs subpopulations analyzed via scRNA-seq. $^{*}P < 0.05$, $^{****}P < 0.0001$ based on two-sided Wilcoxon rank-sum tests. (**g**) The pseudotime kinetics of Cxcl9 and Aplnr across trajectory from state 5 to states 1 and 6. (**h**) Fold changes of Aplnr expression in siNC- and siAplnr-treated bEnd.3 ECs. Data are represented as mean ± SEM, $^{*}P < 0.05$ based on Student's t test, $n = 3$ biological replicates for siNC group and $n = 4$ for siAplnr group. (**i-j**) Analysis of the effect of Aplnr knockdown on cellular metabolism of bEnd.3 cells using Seahorse XF Cell Mito Stress Assay (**i**) and Glycolysis Stress Assay kit (**j**). Data are represented as mean ± SEM, $^{*}P < 0.05$ based on Student's t test, $n = 3$ biological replicates for siNC group and $n = 4$ for siAplnr group. (**k**) Tube formation assay conducted using bEnd.3 ECs with or without siAplnr treatment. The total branching length and the number of meshes are measured and compared by Angiogenesis Analyzer plugin in imageJ. Three randomly selected microscope fields in each well ($n = 3$ per group) are assessed. Data are represented as mean ± SEM, $^{*}P < 0.05$, $^{**}P < 0.01$ by Student's t test. Scale bar: 100 μm

Discussion

In this study, we identified a reduced proportion of venular EC, deteriorated metabolism and enhanced cytokine responses as the key features of aged microvascular ECs. In the microvascular network of the subcutaneous adipose tissue, the proportion of venular ECs was selectively reduced, primarily due to their significantly higher decrease in proliferation score compared to other EC subtypes. Additionally, we observed a pseudotemporal shift in aged ECs, especially those comprising the venular subtype, towards a terminal state. This alteration was linked to reduced oxidative phosphorylation and increased cytokine signaling. Cxcl9 emerged as an inflammatory biomarker of aging-related EC dysfunction, playing a deteriorating role in the energy metabolism and angiogenesis of ECs. Finally, we revealed that Cxcl9-mediated downregulation of Aplnr expression at least partially contributed to the metabolic reprogramming and impaired angiogenesis of ECs observed in aged microvasculature. Our findings suggest that targeting Cxcl9 signaling could be a promising therapeutic strategy for EC dysfunction in elderly microvasculature.

Several studies have documented a reduction in vascular density within the microvasculature of aged individuals [6]. Moreover, it has been reported that microvascular rarefaction can indeed occur in specific segments of the vascular network without uniformly affecting the entire network upon aging. For example, research has revealed a decline in the number of venules and arterioles in the cerebral microvasculature of rats [55] and mice [56], as well as a reduction in capillary density, length, and volume in various regions of the rat brain with advancing age [57, 58]. A recent study using optical coherence tomography and two-photon microscopy demonstrated that brain arteriole and venule at specific dimensions exhibited negative correlations in quantitative parameters between nonaged and aged mice [56]. Our scRNA-seq data further revealed that Thbs1 [51] and Rgcc [52], two negative regulator of EC proliferation, were up-regulated either most significantly or exclusively in venular ECs. This finding may explain the higher susceptibility of venular ECs to aging-related changes compared to other EC subtypes. Further investigation into the molecular pathways regulating Thbs1 and Rgcc expression is warranted in future studies.

Our study demonstrated that all specialized aged EC subtypes underwent a shift to the terminal state, characterized by reduced oxidative phosphorylation and enhanced cytokine signaling. Although glycolysis is traditionally considered the main ATP supplier in healthy ECs [25], recent evidence has revealed that both oxidative phosphorylation and glycolysis play vital roles in EC functions [59]. Glycolysis is strongly associated with angiogenesis, and reduced glycolysis in aged ECs may explain the observed decrease in vascular density [60, 61]. Mitochondrial respiration is highly correlated with EC proliferation and homeostasis; its inhibition suppresses EC proliferation, induces retinal angiogenesis [62], and is linked to the disruption of EC-mediated vascular tone [63]. Moreover, the respiratory pathways of ECs vary across various tissues and are altered under pathological conditions such as the aging process [59, 61]. For instance, in brain ECs, the number of mitochondria is twice that in other ECs [64], and inhibition of oxidative phosphorylation is a critical event in brain microvascular aging [65]. Senescent ECs also undergo senescence-associated metabolic shifts, with decreased glycolysis and oxidative phosphorylation [66]. Our study revealed that the terminal-state transition of aged ECs predominantly affected the venular ECs subtype, indicating that metabolic reprogramming may be linked to aging-associated microvascular structural remodeling.

We observed the dual effects of Cxcl9 on EC metabolism, involving its strongest positive correlation with multiple enzymes involved in fatty acid metabolism, and the most pronounced negative association with the TCA cycle enzyme IDH in aging ECs. Cxcl9, involved in immune responses and inflammation, is secreted by various cells, including interferon-gamma (IFN-γ) stimulated ECs. CXCR3, the receptor for Cxcl9, is a G protein-coupled receptor mainly found in immune cells and facilitates chemotaxis and immune responses. Although the potential roles of Cxcl9 in inhibiting vascular proliferation and promoting EC apoptosis were reported [67, 68], the underlying mechanisms remain unclear. A recent study using a deep learning model linked Cxcl9 to cardiovascular aging demonstrated that silencing CXCL9 can counteract cellular senescence and restore vascular regenerative capacity in human induced pluripotent stem cell (iPSC)-derived aging ECs [69]. Their fast GSEA (FGSEA) results predicted that the downregulated genes were enriched in the hallmark oxidative phosphorylation pathway, and the knockdown of CXCL9 revealed a complete reversal. Our findings validate that Cxcl9 serves as a potential biomarker and key inducer of oxidative phosphorylation and glycolytic dysfunction in ECs, positioning it as a potential therapeutic target for addressing metabolic remodeling during microvascular aging.

Moreover, our study also revealed that Cxcl9-mediated suppression of Aplnr was demonstrated to play a role in regulating the energy metabolism in ECs. Aplnr is a G protein-coupled receptor of Apelin. Apelin peptide-induced Aplnr activation exhibits a wide range of physiological effects [70], including vasodilation [71], myocardial contractility [72], angiogenesis [73], fluid homeostasis, and energy metabolism [74], and protects against cardiovascular defects and

vascular diseases, such as hypertension and atherosclerosis [75, 76]. Apelin/Aplnr signaling plays a significant role in promoting the sprouting of ECs through c-Myc upregulation [73], stimulating nitric oxide (NO) production for vasorelaxation [77], modulating EC polarization through Klf2 [78], controlling venous EC proliferation [79], and inhibiting LPS-induced endothelial mesenchymal transition by promoting ACE2 [80]. Moreover, Aplnr is involved in the regulation of EC metabolism; reduced expression of this factor can inhibit glucose transport [81], glycolysis [73] and fatty acid oxidation [82], and promote fatty acid uptake [81] in ECs. The inactivation of FOXO1 and inhibition of endothelial FABP4 expression act as key downstream targets for apelin/APLNR signaling [81]. Furthermore, the apelin/Aplnr axis has anti-aging properties; its downregulation correlates with accelerated aging in mice, whereas its restoration extends the health span [83]; this effect highlights its potential in combating age-related decline. Our results indicate a novel regulatory link between Cxcl9 and Aplnr signaling in the context of EC energy metabolism and angiogenesis. These findings suggest that targeting inflammatory factors, such as Cxcl9, is a potentially effective strategy for mitigating the effects of aging on vascular metabolism or reversing Aplnr-related endothelial dysfunction.

This study had several limitations. Firstly, we included only 18-month-old female mice with a small sample size ($n=4$). However, sex-related differences have been observed in the aged mice. A previous study revealed that middle-aged female mice show a greater age-related increase in adipose CD8+T cells than middle-aged male mice [84]. Moreover, aging is a chronic and continuous process, and mice over 24 months of age (advanced aging stage) show physiological characteristics differing from those at 18 months of age (early aging stage) [85, 86]. Hence, in the future, both male and female mice at an advanced aging stage with a larger sample size should be analyzed to clarify variations in different phases of aging in the SAT microvasculature. Secondly, we focused on the microvascular network in the SAT of mice, whereas, the aging dynamics of microvascular ECs may significantly differ across various tissues and between mice and humans. This underscores the need for further investigation to ascertain whether the aging features of microvascular ECs in the SAT can be extrapolated to other tissues.

In conclusion, using a combination of scRNA-seq analysis with cytohistological validation, we showed that a reduced proportion of venular EC, deteriorated metabolism and enhanced cytokine responses may be the key features of aged microvascular ECs. Enhanced Cxcl9 expressions may contribute to the metabolic reprogramming and impaired angiogenesis of ECs in aged microvasculature, potentially by suppressing Aplnr expression. Intervening in this pathway may therefore be a promising therapeutic strategy for EC dysfunction in elderly microvasculature.

Supplementary Information The online version contains supplementary material available at https://doi.org/10.1007/s10456-025-09970-y.

Acknowledgements R.X. discloses support from the Chinese Academy of Medical Sciences Innovation Fund for Medical Sciences (CIFMS, grant no. 2021-I2M-1-052) and the National Natural Science Foundation of China (32370884, 81873666).

Author contributions All authors reviewed the manuscript. X.F., Y.Z., and X.C. conducted experiments. X.F., Y.Z., X.C., S.H., C.L., Y.L., F.G., Z.Y., X.Y., R.X. analyzed the data, X.F., Y.Z., X.C. and R.X. wrote the manuscript.

Data availability The scRNA-sequencing data generated in this study are available under the accession codes GSE211742. All data are available in the main text or the supplementary materials.

Declarations

Competing interests The authors declare no competing interests.

References

1. Donato AJ, Machin DR, Lesniewski LA (2018) Mechanisms of dysfunction in the Aging vasculature and role in Age-Related Disease. Circ Res 123(7):825–848. https://doi.org/10.1161/circresaha.118.312563
2. Tyrrell DJ, Goldstein DR (2021) Ageing and atherosclerosis: vascular intrinsic and extrinsic factors and potential role of IL-6. Nat Rev Cardiol 18(1):58–68. https://doi.org/10.1038/s41569-020-0431-7
3. Mengozzi A, Pugliese NR, Chiriacò M, Masi S, Virdis A, Taddei S (2021) Microvascular ageing links metabolic disease to Age-Related disorders: the role of oxidative stress and inflammation in promoting Microvascular Dysfunction. J Cardiovasc Pharmacol 78(Suppl 6):S78–s87. https://doi.org/10.1097/fjc.0000000000001109
4. Ungvari Z, Tarantini S, Donato AJ, Galvan V, Csiszar A (2018) Mechanisms of vascular aging. Circ Res 123(7):849–867. https://doi.org/10.1161/CIRCRESAHA.118.311378

5. Masi S, Georgiopoulos G, Chiriaco M, Grassi G, Seravalle G, Savoia C, Volpe M, Taddei S, Rizzoni D, Virdis A (2020) The importance of endothelial dysfunction in resistance artery remodelling and cardiovascular risk. Cardiovasc Res 116(2):429–437. https://doi.org/10.1093/cvr/cvz096
6. Ungvari Z, Tarantini S, Kiss T, Wren JD, Giles CB, Griffin CT, Murfee WL, Pacher P, Csiszar A (2018) Endothelial dysfunction and angiogenesis impairment in the ageing vasculature. Nat Rev Cardiol 15(9):555–565. https://doi.org/10.1038/s41569-018-0030-z
7. Masi S, Rizzoni D, Taddei S, Widmer RJ, Montezano AC, Luscher TF, Schiffrin EL, Touyz RM, Paneni F, Lerman A, Lanza GA, Virdis A (2021) Assessment and pathophysiology of microvascular disease: recent progress and clinical implications. Eur Heart J 42(26):2590–2604. https://doi.org/10.1093/eurheartj/ehaa857
8. Guven G, Hilty MP, Ince C (2020) Microcirculation: physiology, pathophysiology, and clinical application. Blood Purif 49(1–2):143–150. https://doi.org/10.1159/000503775
9. Scioli MG, Bielli A, Arcuri G, Ferlosio A, Orlandi A (2014) Ageing and microvasculature. Vasc Cell 6:19. https://doi.org/10.1186/2045-824X-6-19
10. Alba C, Vidal L, Diaz F, Villena A, de Vargas IP (2004) Ultrastructural and quantitative age-related changes in capillaries of the dorsal lateral geniculate nucleus. Brain Res Bull 64(2):145–153. https://doi.org/10.1016/j.brainresbull.2004.06.006
11. Le Couteur DG, Fraser R, Cogger VC, McLean AJ (2002) Hepatic pseudocapillarisation and atherosclerosis in ageing. Lancet 359(9317):1612–1615. https://doi.org/10.1016/S0140-6736(02)08524-0
12. Satoh M, Kidokoro K, Ozeki M, Nagasu H, Nishi Y, Ihoriya C, Fujimoto S, Sasaki T, Kashihara N (2013) Angiostatin production increases in response to decreased nitric oxide in aging rat kidney. Lab Invest 93(3):334–343. https://doi.org/10.1038/labinvest.2012.171
13. Kang DH, Anderson S, Kim YG, Mazzalli M, Suga S, Jefferson JA, Gordon KL, Oyama TT, Hughes J, Hugo C, Kerjaschki D, Schreiner GF, Johnson RJ (2001) Impaired angiogenesis in the aging kidney: vascular endothelial growth factor and thrombospondin-1 in renal disease. Am J Kidney Dis 37(3):601–611. https://doi.org/10.1053/ajkd.2001.22087
14. Grunewald M, Kumar S, Sharife H, Volinsky E, Gileles-Hillel A, Licht T, Permyakova A, Hinden L, Azar S, Friedmann Y, Kupetz P, Tzuberi R, Anisimov A, Alitalo K, Horwitz M, Leebhoff S, Khoma OZ, Hlushchuk R, Djonov V, Abramovitch R, Tam J, Keshet E (2021) Counteracting age-related VEGF signaling insufficiency promotes healthy aging and extends life span. Science 373(6554). https://doi.org/10.1126/science.abc8479
15. Zhang W, Zhang S, Yan P, Ren J, Song M, Li J, Lei J, Pan H, Wang S, Ma X, Ma S, Li H, Sun F, Wan H, Li W, Chan P, Zhou Q, Liu GH, Tang F, Qu J (2020) A single-cell transcriptomic landscape of primate arterial aging. Nat Commun 11(1):2202. https://doi.org/10.1038/s41467-020-15997-0
16. Kiss T, Nyul-Toth A, Balasubramanian P, Tarantini S, Ahire C, DelFavero J, Yabluchanskiy A, Csipo T, Farkas E, Wiley G, Garman L, Csiszar A, Ungvari Z (2020) Single-cell RNA sequencing identifies senescent cerebromicrovascular endothelial cells in the aged mouse brain. Geroscience 42(2):429–444. https://doi.org/10.1007/s11357-020-00177-1
17. Zhao L, Li Z, Vong JSL, Chen X, Lai HM, Yan LYC, Huang J, Sy SKH, Tian X, Huang Y, Chan HYE, So HC, Ng WL, Tang Y, Lin WJ, Mok VCT, Ko H (2020) Pharmacologically reversible zonation-dependent endothelial cell transcriptomic changes with neurodegenerative disease associations in the aged brain. Nat Commun 11(1):4413. https://doi.org/10.1038/s41467-020-18249-3
18. Ichijo R, Maki K, Kabata M, Murata T, Nagasaka A, Ishihara S, Haga H, Honda T, Adachi T, Yamamoto T, Toyoshima F (2022) Vasculature atrophy causes a stiffened microenvironment that augments epidermal stem cell differentiation in aged skin. Nat Aging 2(7):592–600. https://doi.org/10.1038/s43587-022-00244-6
19. Pacinella G, Ciaccio AM, Tuttolomondo A (2022) Endothelial dysfunction and chronic inflammation: the cornerstones of vascular alterations in Age-Related diseases. Int J Mol Sci 23(24). https://doi.org/10.3390/ijms232415722
20. Ajoolabady A, Pratico D, Vinciguerra M, Lip GYH, Franceschi C, Ren J (2023) Inflammaging: mechanisms and role in the cardiac and vasculature. Trends Endocrinol Metab 34(6):373–387. https://doi.org/10.1016/j.tem.2023.03.005
21. Khan SY, Awad EM, Oszwald A, Mayr M, Yin X, Waltenberger B, Stuppner H, Lipovac M, Uhrin P, Breuss JM (2017) Premature senescence of endothelial cells upon chronic exposure to TNFalpha can be prevented by N-acetyl cysteine and plumericin. Sci Rep 7:39501. https://doi.org/10.1038/srep39501
22. Zhang L, Liu M, Liu W, Hu C, Li H, Deng J, Cao Q, Wang Y, Hu W, Li Q (2021) Th17/IL-17 induces endothelial cell senescence via activation of NF-kappaB/p53/Rb signaling pathway. Lab Invest 101(11):1418–1426. https://doi.org/10.1038/s41374-021-00629-y
23. Mengozzi A, de Ciuceis C, Dell'oro R, Georgiopoulos G, Lazaridis A, Nosalski R, Pavlidis G, Tual-Chalot S, Agabiti-Rosei C, Anyfanti P, Camargo LL, Dabrowska E, Quarti-Trevano F, Hellmann M, Masi S, Mavraganis G, Montezano AC, Rios FJ, Winklewski PJ, Wolf J, Costantino S, Gkaliagkousi E, Grassi G, Guzik TJ, Ikonomidis I, Narkiewicz K, Paneni F, Rizzoni D, Stamatelopoulos K, Stellos K, Taddei S, Touyz RM, Triantafyllou A, Virdis A (2023) The importance of microvascular inflammation in ageing and age-related diseases: a position paper from the ESH working group on small arteries, section of microvascular inflammation. J Hypertens 41(10):1521–1543. https://doi.org/10.1097/HJH.0000000000003503
24. Ali L, Schnitzler JG, Kroon J (2018) Metabolism: the road to inflammation and atherosclerosis. Curr Opin Lipidol 29(6):474–480. https://doi.org/10.1097/MOL.0000000000000550
25. Li X, Sun X, Carmeliet P (2019) Hallmarks of endothelial cell metabolism in Health and Disease. Cell Metab 30(3):414–433. https://doi.org/10.1016/j.cmet.2019.08.011
26. Choi SJ, Piao S, Nagar H, Jung SB, Kim S, Lee I, Kim SM, Song HJ, Shin N, Kim DW, Irani K, Jeon BH, Park JW, Kim CS (2018) Isocitrate dehydrogenase 2 deficiency induces endothelial inflammation via p66sh-mediated mitochondrial oxidative stress. Biochem Biophys Res Commun 503(3):1805–1811. https://doi.org/10.1016/j.bbrc.2018.07.117
27. Stabenow LK, Zibrova D, Ender C, Helbing DL, Spengler K, Marx C, Wang ZQ, Heller R (2022) Oxidative glucose metabolism promotes senescence in vascular endothelial cells. Cells 11(14). https://doi.org/10.3390/cells11142213
28. Lin T, Yang WQ, Luo WW, Zhang LL, Mai YQ, Li ZQ, Liu ST, Jiang LJ, Liu PQ, Li ZM (2022) Disturbance of Fatty Acid Metabolism Promoted Vascular Endothelial Cell Senescence via Acetyl-CoA-Induced Protein Acetylation Modification. Oxid Med Cell Longev 2022:1198607. https://doi.org/10.1155/2022/1198607
29. You Y, Sun X, Xiao J, Chen Y, Chen X, Pang J, Mi J, Tang Y, Liu Q, Ling W (2022) Inhibition of S-adenosylhomocysteine hydrolase induces endothelial senescence via hTERT downregulation. Atherosclerosis 353:1–10. https://doi.org/10.1016/j.atherosclerosis.2022.06.002
30. Bierhansl L, Conradi LC, Treps L, Dewerchin M, Carmeliet P (2017) Central role of metabolism in endothelial cell function and

vascular disease. Physiol (Bethesda) 32(2):126–140. https://doi.org/10.1152/physiol.00031.2016
31. Sabbatinelli J, Prattichizzo F, Olivieri F, Procopio AD, Rippo MR, Giuliani A (2019) Where metabolism meets senescence: focus on endothelial cells. Front Physiol 10:1523. https://doi.org/10.3389/fphys.2019.01523
32. Cai Z, He B (2023) Adipose tissue aging: an update on mechanisms and therapeutic strategies. Metabolism 138:155328. https://doi.org/10.1016/j.metabol.2022.155328
33. Palmer AK, Kirkland JL (2016) Aging and adipose tissue: potential interventions for diabetes and regenerative medicine. Exp Gerontol 86:97–105. https://doi.org/10.1016/j.exger.2016.02.013
34. Chen S, Pan X, Gao P, Wu F (2024) Single-nucleus transcriptome analysis identifies a novel FKBP5 + endothelial cell subtype involved in endothelial-to-mesenchymal transition in adipose tissue during aging. Biochem Biophys Res Commun 722:150157. https://doi.org/10.1016/j.bbrc.2024.150157
35. Cao Y, Wang H, Wang Q, Han X, Zeng W (2018) Three-dimensional volume fluorescence-imaging of vascular plasticity in adipose tissues. Mol Metab 14:71–81. https://doi.org/10.1016/j.molmet.2018.06.004
36. Frueh FS, Später T, Scheuer C, Menger MD, Laschke MW (2017) Isolation of Murine Adipose Tissue-derived Microvascular Fragments as Vascularization Units for Tissue Engineering. J Vis Exp (122). https://doi.org/10.3791/55721
37. Wolock SL, Lopez R, Klein AM (2019) Scrublet: computational identification of cell doublets in single-cell Transcriptomic Data. Cell Syst 8(4):281–291e289. https://doi.org/10.1016/j.cels.2018.11.005
38. McGinnis CS, Murrow LM, Gartner ZJ (2019) DoubletFinder: Doublet Detection in single-cell RNA sequencing data using Artificial Nearest neighbors. Cell Syst 8(4):329–337e324. https://doi.org/10.1016/j.cels.2019.03.003
39. Butler A, Hoffman P, Smibert P, Papalexi E, Satija R (2018) Integrating single-cell transcriptomic data across different conditions, technologies, and species. Nat Biotechnol 36(5):411–420. https://doi.org/10.1038/nbt.4096
40. Stuart T, Butler A, Hoffman P, Hafemeister C, Papalexi E, Mauck WM 3rd, Hao Y, Stoeckius M, Smibert P, Satija R (2019) Comprehensive Integration of Single-Cell Data. Cell 177(7):1888–1902e1821. https://doi.org/10.1016/j.cell.2019.05.031
41. Korsunsky I, Millard N, Fan J, Slowikowski K, Zhang F, Wei K, Baglaenko Y, Brenner M, Loh PR, Raychaudhuri S (2019) Fast, sensitive and accurate integration of single-cell data with Harmony. Nat Methods 16(12):1289–1296. https://doi.org/10.1038/s41592-019-0619-0
42. Yu G, Wang LG, Han Y, He QY (2012) clusterProfiler: an R package for comparing biological themes among gene clusters. Omics 16(5):284–287. https://doi.org/10.1089/omi.2011.0118
43. Trapnell C, Cacchiarelli D, Grimsby J, Pokharel P, Li S, Morse M, Lennon NJ, Livak KJ, Mikkelsen TS, Rinn JL (2014) The dynamics and regulators of cell fate decisions are revealed by pseudotemporal ordering of single cells. Nat Biotechnol 32(4):381–386. https://doi.org/10.1038/nbt.2859
44. Teschendorff AE, Enver T (2017) Single-cell entropy for accurate estimation of differentiation potency from a cell's transcriptome. Nat Commun 8:15599. https://doi.org/10.1038/ncomms15599
45. Efremova M, Vento-Tormo M, Teichmann SA, Vento-Tormo R (2020) CellPhoneDB: inferring cell-cell communication from combined expression of multi-subunit ligand-receptor complexes. Nat Protoc 15(4):1484–1506. https://doi.org/10.1038/s41596-020-0292-x
46. Wagner A, Wang C, Fessler J, DeTomaso D, Avila-Pacheco J, Kaminski J, Zaghouani S, Christian E, Thakore P, Schellhaass B, Akama-Garren E, Pierce K, Singh V, Ron-Harel N, Douglas VP, Bod L, Schnell A, Puleston D, Sobel RA, Haigis M, Pearce EL, Soleimani M, Clish C, Regev A, Kuchroo VK, Yosef N (2021) Metabolic modeling of single Th17 cells reveals regulators of autoimmunity. Cell 184(16):4168–4185e4121. https://doi.org/10.1016/j.cell.2021.05.045
47. Dobner S, Toth F, de Rooij L (2024) A high-resolution view of the heterogeneous aging endothelium. Angiogenesis 27(2):129–145. https://doi.org/10.1007/s10456-023-09904-6
48. He Y, Tacconi C, Dieterich LC, Kim J, Restivo G, Gousopoulos E, Lindenblatt N, Levesque MP, Claassen M, Detmar M (2022) Novel blood vascular endothelial subtype-specific markers in human skin unearthed by single-cell transcriptomic profiling. Cells 11(7). https://doi.org/10.3390/cells11071111
49. Thiriot A, Perdomo C, Cheng G, Novitzky-Basso I, McArdle S, Kishimoto JK, Barreiro O, Mazo I, Triboulet R, Ley K, Rot A, von Andrian UH (2017) Differential DARC/ACKR1 expression distinguishes venular from non-venular endothelial cells in murine tissues. BMC Biol 15(1):45. https://doi.org/10.1186/s12915-017-0381-7
50. Girbl T, Lenn T, Perez L, Rolas L, Barkaway A, Thiriot A, Del Fresno C, Lynam E, Hub E, Thelen M, Graham G, Alon R, Sancho D, von Andrian UH, Voisin MB, Rot A, Nourshargh S (2018) Distinct Compartmentalization of the Chemokines CXCL1 and CXCL2 and the Atypical Receptor ACKR1 Determine Discrete Stages of Neutrophil Diapedesis. Immunity 49(6):1062–1076.e6. https://doi.org/10.1016/j.immuni.2018.09.018
51. Gao Q, Chen K, Gao L, Zheng Y, Yang YG (2016) Thrombospondin-1 signaling through CD47 inhibits cell cycle progression and induces senescence in endothelial cells. Cell Death Dis 7(9):e2368. https://doi.org/10.1038/cddis.2016.155
52. Voigt AP, Mulfaul K, Mullin NK, Flamme-Wiese MJ, Giacalone JC, Stone EM, Tucker BA, Scheetz TE, Mullins RF (2019) Single-cell transcriptomics of the human retinal pigment epithelium and choroid in health and macular degeneration. Proc Natl Acad Sci U S A 116(48):24100–24107. https://doi.org/10.1073/pnas.1914143116
53. Chrobak I, Lenna S, Stawski L, Trojanowska M (2013) Interferon-gamma promotes vascular remodeling in human microvascular endothelial cells by upregulating endothelin (ET)-1 and transforming growth factor (TGF) beta2. J Cell Physiol 228(8):1774–1783. https://doi.org/10.1002/jcp.24337
54. Rossin D, Vanni R, Lo Iacono M, Cristallini C, Giachino C, Rastaldo R (2023) APJ as Promising Therapeutic target of peptide analogues in myocardial infarction- and Hypertension-Induced Heart failure. Pharmaceutics 15(5). https://doi.org/10.3390/pharmaceutics15051408
55. Sonntag WE, Lynch CD, Cooney PT, Hutchins PM (1997) Decreases in cerebral microvasculature with age are associated with the decline in growth hormone and insulin-like growth factor 1. Endocrinology 138(8):3515–3520. https://doi.org/10.1210/endo.138.8.5330
56. Yan F, Alhajeri ZA, Nyul-Toth A, Wang C, Zhang Q, Mercyshalinie ERS, Delfavero J, Ahire C, Mutembei BM, Tarantini S, Csiszar A, Tang Q (2024) Dimension-based quantification of aging-associated cerebral microvasculature determined by optical coherence tomography and two-photon microscopy. J Biophotonics 17(3):e202300409. https://doi.org/10.1002/jbio.202300409
57. Zhang R, Kadar T, Sirimanne E, MacGibbon A, Guan J (2012) Age-related memory decline is associated with vascular and microglial degeneration in aged rats. Behav Brain Res 235(2):210–217. https://doi.org/10.1016/j.bbr.2012.08.002
58. Shao WH, Li C, Chen L, Qiu X, Zhang W, Huang CX, Xia L, Kong JM, Tang Y (2010) Stereological investigation of age-related changes of the capillaries in white matter. Anat Rec (Hoboken) 293(8):1400–1407. https://doi.org/10.1002/ar.21184

59. Falkenberg KD, Rohlenova K, Luo Y, Carmeliet P (2019) The metabolic engine of endothelial cells. Nat Metab 1(10):937–946. https://doi.org/10.1038/s42255-019-0117-9
60. De Bock K, Georgiadou M, Schoors S, Kuchnio A, Wong BW, Cantelmo AR, Quaegebeur A, Ghesquiere B, Cauwenberghs S, Eelen G, Phng LK, Betz I, Tembuyser B, Brepoels K, Welti J, Geudens I, Segura I, Cruys B, Bifari F, Decimo I, Blanco R, Wyns S, Vangindertael J, Rocha S, Collins RT, Munck S, Daelemans D, Imamura H, Devlieger R, Rider M, Van Veldhoven PP, Schuit F, Bartrons R, Hofkens J, Fraisl P, Telang S, Deberardinis RJ, Schoonjans L, Vinckier S, Chesney J, Gerhardt H, Dewerchin M, Carmeliet P (2013) Role of PFKFB3-driven glycolysis in vessel sprouting. Cell 154(3):651–663. https://doi.org/10.1016/j.cell.2013.06.037
61. Dumas SJ, Garcia-Caballero M, Carmeliet P (2020) Metabolic signatures of distinct endothelial phenotypes. Trends Endocrinol Metab 31(8):580–595. https://doi.org/10.1016/j.tem.2020.05.009
62. Diebold LP, Gil HJ, Gao P, Martinez CA, Weinberg SE, Chandel NS (2019) Mitochondrial complex III is necessary for endothelial cell proliferation during angiogenesis. Nat Metab 1(1):158–171. https://doi.org/10.1038/s42255-018-0011-x
63. Wilson C, Lee MD, Buckley C, Zhang X, McCarron JG (2023) Mitochondrial ATP production is required for endothelial cell control of vascular tone. Function (Oxf) 4(2):zqac063. https://doi.org/10.1093/function/zqac063
64. Oldendorf WH, Cornford ME, Brown WJ (1977) The large apparent work capability of the blood-brain barrier: a study of the mitochondrial content of capillary endothelial cells in brain and other tissues of the rat. Ann Neurol 1(5):409–417. https://doi.org/10.1002/ana.410010502
65. Sakamuri SS, Sure VN, Kolli L, Evans WR, Sperling JA, Bix GJ, Wang X, Atochin DN, Murfee WL, Mostany R, Katakam PV (2022) Aging related impairment of brain microvascular bioenergetics involves oxidative phosphorylation and glycolytic pathways. J Cereb Blood Flow Metab 42(8):1410–1424. https://doi.org/10.1177/0271678X211069266
66. Hwang HJ, Kim N, Herman AB, Gorospe M, Lee JS (2022) Factors and pathways modulating endothelial cell senescence in vascular aging. Int J Mol Sci 23(17). https://doi.org/10.3390/ijms231710135
67. Cunningham CM, Li M, Ruffenach G, Doshi M, Aryan L, Hong J, Park J, Hrncir H, Medzikovic L, Umar S, Arnold AP, Eghbali M (2022) Y-Chromosome gene, Uty, protects against pulmonary hypertension by reducing Proinflammatory chemokines. Am J Respir Crit Care Med 206(2):186–196. https://doi.org/10.1164/rccm.202110-2309OC
68. Huang B, Wang W, Li Q, Wang Z, Yan B, Zhang Z, Wang L, Huang M, Jia C, Lu J, Liu S, Chen H, Li M, Cai D, Jiang Y, Jin D, Bai X (2016) Osteoblasts secrete Cxcl9 to regulate angiogenesis in bone. Nat Commun 7:13885. https://doi.org/10.1038/ncomms13885
69. Sayed N, Huang Y, Nguyen K, Krejciova-Rajaniemi Z, Grawe AP, Gao T, Tibshirani R, Hastie T, Alpert A, Cui L, Kuznetsova T, Rosenberg-Hasson Y, Ostan R, Monti D, Lehallier B, Shen-Orr SS, Maecker HT, Dekker CL, Wyss-Coray T, Franceschi C, Jojic V, Haddad F, Montoya JG, Wu JC, Davis MM, Furman D (2021) An inflammatory aging clock (iAge) based on deep learning tracks multimorbidity, immunosenescence, frailty and cardiovascular aging. Nat Aging 1:598–615. https://doi.org/10.1038/s43587-021-00082-y
70. Kuba K, Sato T, Imai Y, Yamaguchi T (2019) Apelin and Elabela/Toddler; double ligands for APJ/Apelin receptor in heart development, physiology, and pathology. Peptides 111:62–70. https://doi.org/10.1016/j.peptides.2018.04.011
71. Chapman FA, Maguire JJ, Newby DE, Davenport AP, Dhaun N (2023) Targeting the apelin system for the treatment of cardiovascular diseases. Cardiovasc Res 119(17):2683–2696. https://doi.org/10.1093/cvr/cvad171
72. Perjes A, Skoumal R, Tenhunen O, Konyi A, Simon M, Horvath IG, Kerkela R, Ruskoaho H, Szokodi I (2014) Apelin increases cardiac contractility via protein kinase cepsilon- and extracellular signal-regulated kinase-dependent mechanisms. PLoS ONE 9(4):e93473. https://doi.org/10.1371/journal.pone.0093473
73. Helker CS, Eberlein J, Wilhelm K, Sugino T, Malchow J, Schuermann A, Baumeister S, Kwon HB, Maischein HM, Potente M, Herzog W, Stainier DY (2020) Apelin signaling drives vascular endothelial cells toward a pro-angiogenic state. Elife 9. https://doi.org/10.7554/eLife.55589
74. Hu G, Wang Z, Zhang R, Sun W, Chen X (2021) The role of Apelin/Apelin Receptor in Energy Metabolism and Water Homeostasis: a Comprehensive Narrative Review. Front Physiol 12:632886. https://doi.org/10.3389/fphys.2021.632886
75. Chun HJ, Ali ZA, Kojima Y, Kundu RK, Sheikh AY, Agrawal R, Zheng L, Leeper NJ, Pearl NE, Patterson AJ, Anderson JP, Tsao PS, Lenardo MJ, Ashley EA, Quertermous T (2008) Apelin signaling antagonizes Ang II effects in mouse models of atherosclerosis. J Clin Invest 118(10):3343–3354. https://doi.org/10.1172/jci34871
76. Chapman FA, Nyimanu D, Maguire JJ, Davenport AP, Newby DE, Dhaun N (2021) The therapeutic potential of apelin in kidney disease. Nat Rev Nephrol 17(12):840–853. https://doi.org/10.1038/s41581-021-00461-z
77. Mughal A, Sun C, O'Rourke ST (2018) Activation of large conductance, calcium-activated Potassium channels by nitric oxide mediates Apelin-Induced relaxation of isolated rat coronary arteries. J Pharmacol Exp Ther 366(2):265–273. https://doi.org/10.1124/jpet.118.248682
78. Kwon HB, Wang S, Helker CS, Rasouli SJ, Maischein HM, Offermanns S, Herzog W, Stainier DY (2016) In vivo modulation of endothelial polarization by apelin receptor signalling. Nat Commun 7:11805. https://doi.org/10.1038/ncomms11805
79. Lathen C, Zhang Y, Chow J, Singh M, Lin G, Nigam V, Ashraf YA, Yuan JX, Robbins IM, Thistlethwaite PA (2014) ERG-APLNR axis controls pulmonary venule endothelial proliferation in pulmonary veno-occlusive disease. Circulation 130(14):1179–1191. https://doi.org/10.1161/CIRCULATIONAHA.113.007822
80. Wang H, Cong L, Yin X, Zhang N, Zhu M, Sun T, Fan J, Xue F, Fan X, Gong Y (2022) The Apelin-APJ axis alleviates LPS-induced pulmonary fibrosis and endothelial mesenchymal transformation in mice by promoting angiotensin-converting enzyme 2. Cell Signal 98:110418. https://doi.org/10.1016/j.cellsig.2022.110418
81. Hwangbo C, Wu J, Papangeli I, Adachi T, Sharma B, Park S, Zhao L, Ju H, Go GW, Cui G, Inayathullah M, Job JK, Rajadas J, Kwei SL, Li MO, Morrison AR, Quertermous T, Mani A, Red-Horse K, Chun HJ (2017) Endothelial APLNR regulates tissue fatty acid uptake and is essential for apelin's glucose-lowering effects. Sci Transl Med 9(407). https://doi.org/10.1126/scitranslmed.aad4000
82. Saleme B, Das SK, Zhang Y, Boukouris AE, Lorenzana Carrillo MA, Jovel J, Wagg CS, Lopaschuk GD, Michelakis ED, Sutendra G (2020) p53-Mediated repression of the PGC1A (PPARG Coactivator 1alpha) and APLNR (apelin receptor) signaling pathways limits fatty acid oxidation energetics: implications for Cardio-Oncology. J Am Heart Assoc 9(15):e017247. https://doi.org/10.1161/JAHA.120.017247
83. Rai R, Ghosh AK, Eren M, Mackie AR, Levine DC, Kim SY, Cedernaes J, Ramirez V, Procissi D, Smith LH, Woodruff TK, Bass J, Vaughan DE (2017) Downregulation of the Apelinergic Axis accelerates aging, whereas its systemic restoration improves the mammalian Healthspan. Cell Rep 21(6):1471–1480. https://doi.org/10.1016/j.celrep.2017.10.057

84. Ahnstedt H, Roy-O'Reilly M, Spychala MS, Mobley AS, Bravo-Alegria J, Chauhan A, Aronowski J, Marrelli SP, McCullough LD (2018) Sex differences in adipose tissue CD8(+) T Cells and Regulatory T Cells in Middle-aged mice. Front Immunol 9:659. https://doi.org/10.3389/fimmu.2018.00659
85. Evans DS, O'Leary MN, Murphy R, Schmidt M, Koenig K, Presley M, Garrett B, Kim HN, Han L, Academia EC, Laye MJ, Edgar D, Zambataro CA, Barhydt T, Dewey CM, Mayfield J, Wilson J, Alavez S, Lucanic M, Kennedy BK, Almeida M, Andersen JK, Kapahi P, Lithgow GJ, Melov S (2021) Longitudinal functional study of murine aging: a resource for future study designs. JBMR Plus 5(3):e10466. https://doi.org/10.1002/jbm4.10466
86. Bennett HC, Zhang Q, Wu YT, Manjila SB, Chon U, Shin D, Vanselow DJ, Pi HJ, Drew PJ, Kim Y (2024) Aging drives cerebrovascular network remodeling and functional changes in the mouse brain. Nat Commun 15(1):6398. https://doi.org/10.1038/s41467-024-50559-8